Facile one pot preparation of magnetic chitosan-palygorskite nanocomposite for efficient removal of lead from water

Published in: *Journal of Colloid and Interface Science*

Citation for published version: Rusmin, R., Sarkar, B., Mukhopadhyay, R., Tsuzuki, T., Liu, Y., Naidu, R., (2022) Facile one pot preparation of magnetic chitosan-palygorskite nanocomposite for efficient removal of lead from water. *Journal of Colloid and Interface Science*, 608(1): 575-587. doi: 10.1016/j.jcis.2021.09.109.

Document version: Accepted peer-reviewed version.

Facile one pot preparation of magnetic chitosan-palygorskite nanocomposite for efficient removal of lead from water

Ruhaida Rusmin[a,b]*, Binoy Sarkar[c]*, Raj Mukhopadhyay[d], Takuya Tsuzuki[e], Yanju Liu [f,g], Ravi Naidu[f,g]

[a] Faculty of Applied Sciences, Universiti Teknologi MARA, Negeri Sembilan Branch, Kuala Pilah Campus, 72000 Kuala Pilah, Negeri Sembilan, Malaysia

[b] Future Industries Institute, University of South Australia, Mawson Lakes, SA 5095, Australia

[c] Lancaster Environment Centre, Lancaster University, Lancaster, LA1 4YQ, UK

[d] Division of Irrigation and Drainage Engineering, ICAR-Central Soil Salinity Research Institute, Karnal – 132001, Haryana, India

[e] Research School of Engineering, College of Engineering and Computer Science, Australian National University, Acton, ACT 2601, Australia

[f] Global Centre for Environmental Remediation, The University of Newcastle, Callaghan, NSW 2308, Australia

[g] Cooperative Research Centre for Contamination Assessment and Remediation of the Environment, ATC Building, Callaghan, NSW 2308, Australia

*Co-corresponding authors: b.sarkar@lancaster.ac.uk (B. Sarkar), ruhaida@uitm.edu.my (R. Rusmin)

Highlights

- Magnetic chitosan-palygorskite (MCP) was fabricated in simple and green method.
- MCP removed 58.5 mg g^{-1} of lead from water.
- Complexation and chemical reduction of lead on MCP surface was evidenced.
- MCP recorded 82% lead removal even following four regeneration cycles.
- MCP retained superparamagnetic nature after regeneration.

Graphical abstract

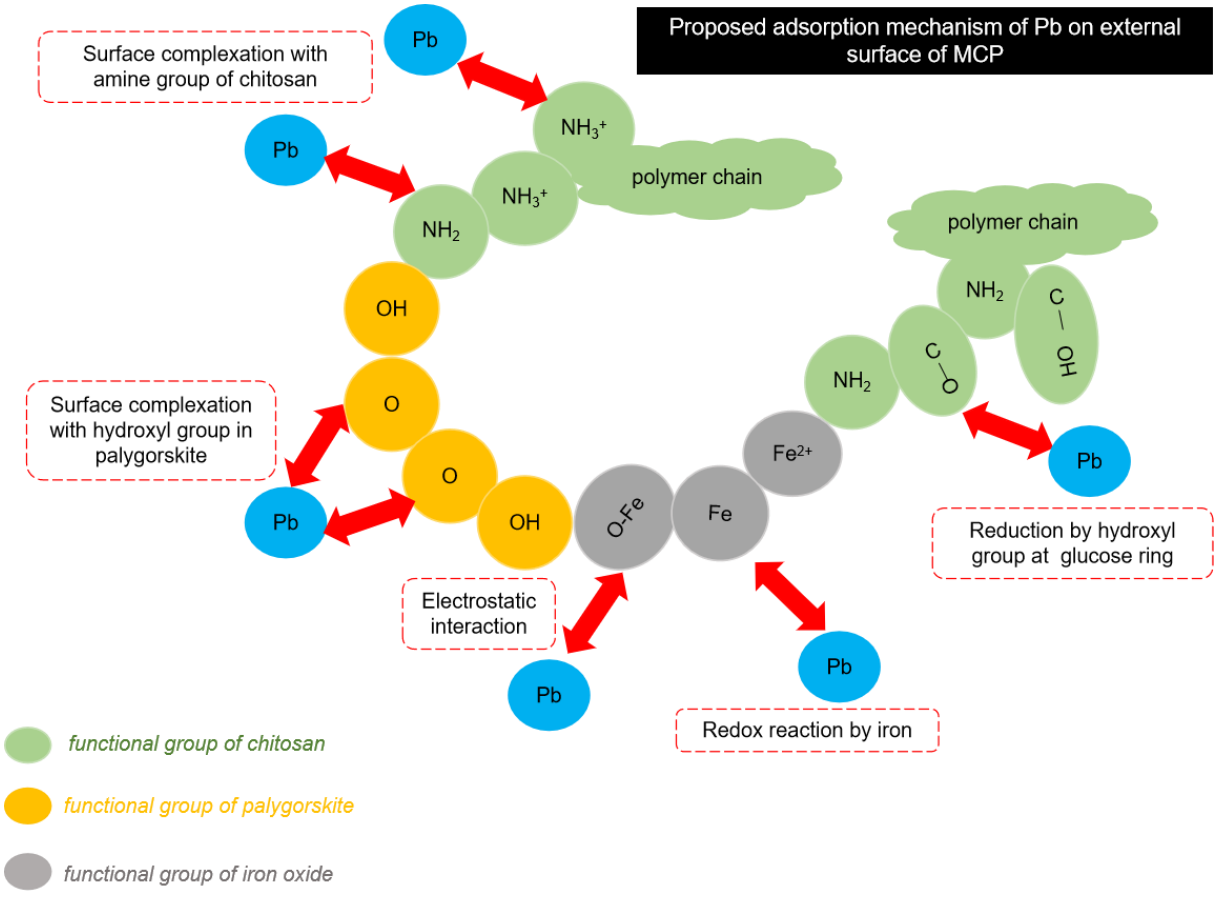

Abstract

Development of polymeric magnetic adsorbents is a promising approach to obtain efficient treatment of contaminated water. However, the synthesis of magnetic composites involving multiple components frequently involves tedious preparation steps. In the present study, a magnetic chitosan-palygorskite (MCP) nanocomposite was prepared through a straight-forward one pot synthesis approach to evaluate its lead (Pb^{2+}) removal capacity from aqueous solution. The nano-architectural and physicochemical properties of the newly-developed MCP composite were described via micro- and nano-morphological analyses, and crystallinity, surface porosity and magnetic susceptibility measurements. The MCP nanocomposite was capable to remove up to 58.5 mg Pb^{2+} g^{-1} of MCP from water with a good agreement of experimental data to the Langmuir isotherm model (R^2 = 0.98). The Pb^{2+} adsorption process on MCP was a multistep diffusion-controlled phenomenon evidenced by the well-fitting of kinetic adsorption data to the intra-particle diffusion model (R^2 = 0.96). Thermodynamic analysis suggested that the adsorption process at low Pb^{2+} concentration was controlled by chemisorption, whereas that at high Pb^{2+} concentration was dominated by physical adsorption. X-ray photoelectron and Fourier transform infrared spectroscopy results suggested that the Pb adsorption on MCP was governed by surface complexation and chemical reduction mechanisms. During regeneration, the MCP retained 82% Pb^{2+} adsorption capacity following four adsorption-desorption cycles with ease to recover the adsorbent using its strong magnetic property. These findings highlight the enhanced structural properties of the easily-prepared nanocomposite which holds outstanding potential to be used as an inexpensive and green adsorbent for remediating Pb^{2+} contaminated water.

Keywords: Adsorbent regeneration; Chitosan; Lead removal; Magnetic nanocomposite; Palygorskite; Wastewater treatment.

1. Introduction

The widespread occurrence of toxic heavy metal contaminants in water resources requires sustainable mitigation strategies to ensure the global water security. Lead (Pb) is one of the major heavy metals that enters into water streams from sources and activities such as battery industries, ceramic industries, e-wastes, mining, printing, pipes, and many others including household activities [1]. Human exposure of Pb through consumption of Pb-contaminated drinking water and food may severely affect the lung, kidney, brain and nervous system [2]. Hence, the United States Environmental Protection Agency (USEPA) fixed the critical concentration of Pb as 0.015 mg L^{-1} in drinking water as a measure to control the fatality and long-term Pb exposure to humans caused by water contamination [3].

Natural adsorbents are regarded as a promising and environmentally benign group of materials for tackling the high cost of resources in treating contaminated water. Naturally available clay minerals such as kaolinite, bentonite, montmorillonite and palygorskite are widely used for the removal of a wide range of contaminants (e.g., heavy metals, dyes, pesticides) from aqueous systems due to the low cost, wide natural abundance, and desirable physico-chemical, thermal and mechanical properties of the mineral materials. The clay minerals have large specific surface area (SSA), high cation exchange capacity (CEC), high thermal stability and numerous surface functional groups useful for interacting with environmental contaminants [4], [5]. Palygorskite, in particular, has been used for heavy metal removal from aqueous solutions and found to be a good inorganic filler material in polymer-clay composite preparation [4], [6], [7], [8]. However, pristine palygorskite suffers from poor adsorption capacity, high desorption rate, and lack of standardized protocol to use [9], [10]. This necessitates the development of novel clay mineral-based functional materials for enhancing the contaminant adsorption and retention capacity while also upholding environmental sustainability in resource utilization.

In this direction, polymer-clay nanocomposites have emerged as one of the promising hybrid materials for developing environmentally friendly adsorbents for wastewater treatment [11]. The incorporation of biopolymers such as chitosan (derived from shrimp and other crustacean organisms) and alginate in polymer-clay nanocomposites is of great environmental interest due to their wide natural abundance and non-toxic nature towards living organisms [12]. Within the composite's structure, clay minerals can provide a support to the biopolymers which often suffer from low mechanical strength and high solubility in acidic solution. Removal of a wide range of organic and inorganic contaminants from wastewater using chitosan-clay composites were reported, including the novel magnetic feature of the composites [13], [14], [15], [16], [17]. For the recovery of spent adsorbent from water, magnetic polymer-clay composites have the advantage of easy magnetic separation via an external magnetic field as opposed to conventional centrifugation and filtration approaches. However, the preparation of magnetic clay nanocomposites involves notably tedious procedures such as pre-synthesis of the magnetic (e.g., iron oxide) nanoparticles, pre-treatment of the clay minerals, and dissolution of the polymer in a suitable solvent followed by cross-linking or precipitation for obtaining the final product [18], [19]. The above multi-step procedure can incur unfavourable operational expenditure, prolong the preparation time of the composite, and cause environmental threat due to excessive use of solvents and auxiliary chemicals. Thus, a straight-forward preparation procedure of magnetic clay nanocomposites is of great interest. To advocate the effectiveness of such green preparation approach, understanding the structural integration of the multidimensional components (i.e., 2D/3D clay minetals, polymeric molecules, and nanosized magnetic particles) within the magnetic polymer-clay nanocomposites is immensely important. In parallel, a systematic assessment of performance of the easily-prepared nanocomposites for removing contaminants from water would ascertain the materials' potential as a new-class of effective adsorbents.

In this study, a facile one-pot *in-situ* preparation of magnetic chitosan-palygorskite (MCP) nanocomposite was achieved by employing a straight-forward, green, and practical synthesis method. The synthesised MCP was characterised through state-of-the-art techniques, such as X-ray diffraction (XRD), Fourier transform infra-red (FTIR) spectroscopy, scanning and transmission electron microscopy (SEM and TEM), thermogravimetric analysis (TGA), X-ray photoelectron spectroscopy (XPS), and surface area, porous structure and magnetism analyses, to gain in-depth understanding of the molecular interactions of each assembled component (i.e., polymer, clay mineral and iron oxide). Furthermore, the MCP was evaluated for its potential application in Pb^{2+} removal from aqueous solutions. The adsorption isotherm profiling, kinetic and thermodynamic studies were performed to postulate the removal mechanisms. Finally, the regeneration feasibility of the nanocomposite was assessed and compared with other similar magnetic nanocomposites.

2. Materials and methods

2.1 Materials and reagents

Chitosan (average molecular weight (MW) 400,000 g mol^{-1}; maximum degree of deacetylation 85%) was purchased from Sigma-Aldrich, Australia. Palygorskite (particle size < 90 μm) originating in Western Australia was purchased from Hudson Resource Pty. Ltd., Australia, and used as received (without purification). Lead (II) nitrate ($Pb(NO_3)_2$, MW = 331.208 g mol^{-1}) and ammonium hydroxide (NH_4OH, ≥ 25% v/v purity) were procured from Fisher Scientific (United Kingdom), iron (III) chloride hexahydrate ($FeCl_3.6H_2O$, MW = 270.30 g mol^{-1}, 99% assay) from Chem-Supply (Australia), iron (II) chloride tetrahydrate ($FeCl_2.4H_2O$, MW = 198.81 g mol^{-1}, 99% assay) from Sigma-Aldrich (Germany), calcium nitrate tetrahydrate ($Ca(NO_3)_2.4H_2O$, MW = 236.15 g mol^{-1}, 99% assay) and sodium nitrate ($NaNO_3$, MW = 84.99 g mol^{-1}, 99% assay) from Bio-Lab (Australia), and

ethylenediaminetetraacetic acid disodium salt (EDTA-Na_2, MW = 198.81 g mol^{-1}, 99% assay) from Sigma-Aldrich (USA). All the reagents were of analytical or laboratory grade.

2.2 Preparation of magnetic chitosan-palygorskite nanocomposite

Palygorskite (0.5 g) was first dispersed in 50 mL of Milli-Q water (resistivity ≥ 18 MΩ.cm) overnight through continuous stirring on a magnetic stirrer (200 rpm). Chitosan solution (0.5 g L^{-1}) in 2% (v/v) acetic acid was prepared under constant stirring (500 rpm) for 2 h at 40°C. The chitosan solution was left to cool at 25°C until all the air bubbles disappeared. On the other hand, $FeCl_3.6H_2O$ (1.086 g) was dissolved in 10 mL Milli-Q water followed by the addition of $FeCl_2.4H_2O$ (0.416 g). The Fe^{3+}-Fe^{2+} (2:1 molar ratio of Fe^{3+}: Fe^{2+}) solution was then immediately transferred to the chitosan solution, and the mixture was stirred rapidly under an N_2 atmosphere at 60°C. The palygorskite suspension was added to the chitosan-Fe^{3+}-Fe^{2+} solution and allowed to react for 90 min at 55 to 60°C upon continuous stirring. Then, 5 mL of NH_4OH (25% (v/v)) was added drop wise to the above mixture upon vigorous stirring for 30 min. The NH_4OH was added in excess (20:1 molar ratio of OH^-: Fe^{2+}/ Fe^{3+}according to stoichiometric conversion to ensure a complete co-precipitation of Fe^{3+}-Fe^{2+} mixture and solidification of the modified chitosan suspension (Eq. 1):

$$2Fe^{3+} + Fe^{2+} + 8OH^- \rightarrow Fe_3O_4 + 4H_2O \qquad \text{(Eq. 1)}$$

The black precipitate of the magnetic chitosan-palygorskite nanocomposite (MCP) was then vacuum-filtered, and washed thoroughly with Milli-Q water and absolute ethanol in turns before drying in a hot-air oven at 40°C overnight. The nanocomposite was grounded in an agate mortar and pestled to pass through a sieve with 90-μm mesh size. For comparison purpose, a pristine iron oxide was prepared using the similar procedure described above without the addition of chitosan and palygorskite.

2.3 Material characterization

X-ray Diffraction (XRD) patterns of powdered samples were collected on a Malvern PANalytical Empyrean diffractometer using CuK_α (λ=1.54 Å) radiation operating at 40 mA and 40 kV in the 2θ range of 4 to 90° with a step size of 0.013 s^{-1} using 0.25° and 0.50° fixed divergence and anti-scatter slits, respectively. Fourier Transform Infra-Red (FTIR) spectra were collected using a Nicolet 6700 series spectrometer (Thermo Scientific) in the range of 4000–400 cm^{-1} wave number by co-addition of 16 scans with a resolution of 8 cm^{-1}. The sample pellets were prepared with dehydrated KBr at a 1:200 (w/w) sample:KBr ratio. The BET (Brunauer–Emmett–Teller) specific surface area (SSA) and BJH (Barrett-Joyner-Halenda) pore size distribution were determined through N_2 adsorption-desorption isotherms at liquid nitrogen temperature (–196°C) on a Micromeritics Gemini 2380 Surface Area Analyser. The samples were degassed overnight at 60°C under vacuum at 2 Torr prior to SSA analysis. Zeta potential was measured (loading of 0.01% m/v) in duplicate on a zeta potential analyser (Nicomp™ 380 ZLS, USA). The magnetic measurement was conducted using a Vibrating Sample Magnetometer (VSM) (MicroMag™ Model 3900 Series). The measurement was conducted in triplicate at 27°C with approximately 10 to 45 mg powdered sample at 1 Tesla and averaging time of 100 to 200 ms. Thermo gravimetric analysis (TGA) was performed using a Mettler Toledo Thermogravimetric Analyser (TGA/DSC 1 model) equipped with STAR^e system with a heating rate of 10°C min^{-1} from 25 to 950°C under N_2 environment (flow rate of 50 mL min^{-1}).

The surface morphology of the nanocomposite was examined by using a FEI Quanta 450 FEG Environmental Scanning Electron Microscope (SEM) equipped with an Apollo X SDD Energy Dispersive X-ray (EDX) detector. A drop of dilute sample suspension (in ethanol) was placed on a silicon wafer that was adhered to double-sided carbon tape and mounted on an aluminium stub. The air-dried samples were coated with pulsed carbon (30 nm thickness)

by a QUORUM Q150T E Carbon Coater. The SEM investigation was conducted in high vacuum (HV) mode using an Everhart-Thornley detector. Meanwhile, the Transmission Electron Microscope (TEM) image was recorded using a JEOL JEM-2100F-HR transmission electron microscope equipped with a field emission gun operated at 200 kV. The Scanning Transmission Electron Microscope (STEM) image of dispersed MCP (in diluted ethanol) was collected by the same instrument using the annular bright field (BF) and dark field (DF) detectors. X-ray Photoelectron Spectroscopy (XPS) analysis was performed on a Kratos AXIS Ultra DLD spectrometer with a monochromatic Al X-ray source at 225 W having a characteristic energy of 1486.6 eV. The analysis was conducted under vacuum ($4x10^{-9}$ Torr) with applied charge neutraliser during the scan. The wide survey scan was performed from 0 with pass energy of 160 eV while for the high-resolution analysis, the pass energy was lowered to 20 eV. Analysis of the binding energy was calibrated with the C_{1s} peak of the aliphatic carbons present at 284.4 eV.

2.4 Adsorption and adsorbent regeneration experiments

The Pb^{2+} stock solution was prepared by dissolving $Pb(NO_3)_2$ in Milli-Q water and diluted to various working concentrations. Batch adsorption experiments were conducted by allowing the MCP to react with aqueous solutions of Pb^{2+} (initial Pb^{2+} concentration ranging from 50 to 500 mg L^{-1}, adsorbent loading 5 g L^{-1}, initial pH 4, at 25°C) in capped polyethylene tubes under reciprocating shaking at 150 agitations per min. The Pb-loaded MCP was recovered magnetically, and the supernatant was filtered through a 0.45 μm membrane filter. The initial and equilibrium concentrations of Pb^{2+} were determined using an Inductively Coupled Plasma Optical Emission Spectrometer (ICP-OES) (Perkin Elmer, Optima 5300V). All experiments were conducted in duplicate, and the mean values are reported. The adsorption of Pb^{2+} on the wall of polyethylene tubes was negligible.

220 The amount of Pb^{2+} adsorbed onto the adsorbent was calculated using Eq. 2:

221 $$q_e = \frac{(C_i - C_e)\,V}{m} \qquad \text{(Eq. 2)}$$

222 where, q_e is the amount of metal adsorbed at equilibrium (mg g^{-1}), C_i and C_e are the initial
223 and equilibrium Pb^{2+} concentrations (mg L^{-1}), respectively, V is the volume (L) of the
224 solution, and m is the mass (g) of the adsorbent.
225 The effect of pH on adsorption was investigated by adjusting the pH (3 to 7) of 50 mg L^{-1}
226 Pb^{2+} solution using 0.01 *M* of HNO_3 or NaOH. The influence of contact time was studied
227 from 10 min to 24 h. The thermodynamic study (temperature effect) was pursued by
228 conducting adsorption experiments at 25, 40 and 55°C with 5 g L^{-1} adsorbent loading at pH 4.
229 The adsorption data were fitted to the Langmuir, Freundlich, Dubinin-Radushkevich (D-R)
230 and Temkin isothermal models (Supplementary Data (SD1)) to understand the adsorption
231 behaviour of Pb^{2+} on MCP. The kinetic adsorption behaviour was evaluated using the pseudo
232 first order, pseudo second order, intra-particle diffusion and Elovich models in order to
233 understand the mechanisms of Pb^{2+} adsorption (SD2). The standard Gibbs free energy change
234 of adsorption (ΔG°) was determined by the classic van't Hoff equation (SD3) to evaluate the
235 effect of temperature on the adsorption process.
236 In the adsorbent regeneration study, the Pb-loaded MCP (initial Pb^{2+} concentration 100 mg
237 L^{-1}) was agitated in a 0.01 M EDTA-Na_2 aqueous solution (adsorbent loading 5 g L^{-1}) for 30
238 min upon reciprocal shaking (150 agitations per min) for four adsorption-desorption cycles.
239 The quantity of desorbed Pb^{2+} was determined by ICP-OES using Eq. 3:

240 $$\text{Desorption } \% = \frac{\text{Amount of Pb desorbed}}{\text{Amount of Pb adsorbed}} \text{x } 100 \qquad \text{(Eq. 3)}$$

241

3. Results and discussion

3.1 Structural and morphological characterization of magnetic chitosan-palygorskite nanocomposite

The characteristic diffraction reflections of palygorskite were observed at 2θ = 8.5° (10.39 Å), 19.6° (4.52 Å) and 24.9° (3.57 Å) accompanied by reflections of kaolinite at 2θ = 12.3° (7.19 Å), and quartz at 2θ = 20.8° (4.27 Å) and 26.4° (3.37 Å) (Fig. 1 a) [20]. A sharp reflection at 2θ = 30.8° was assigned to dolomite (calcium magnesium carbonate) which was an impurity in the pristine palygorskite. Meanwhile, the iron oxide showed characteristics reflections at 2θ positions of 30.1°, 35.5°, 43.1° 53.4°, 57.0°, and 62.6°, which corresponded to (220), (311), (400), (422), (511) and (440) diffraction planes of magnetite (Fe_3O_4) respectively (International Centre for Diffraction Data (ICDD®) File No. 04-008-8146) [21]. Chitosan is amorphous in nature. The diffraction pattern of the MCP coincided with the patterns of the magnetite and palygorskite (Fig. 1 a) except for a broad reflection at 2θ =10.39 Å due to incorporation of the amorphous chitosan component in the nanocomposite, as similarly observed in other chitosan-palygorskite nanocomposites [4], [22]. The dolomite reflection (2θ = 30.8°) was absent in MCP (Fig. 1 a), which indicated that the acidic $Fe^{2+/}Fe^{3+}$ suspension (pH=2.1) at initial stage of the synthesis removed the carbonate impurity such as dolomite from the clay mineral.

When a permanent magnet (AlNiCo bar magnet) was placed close to the wall of a vial containing an aqueous suspension of MCP, the particles were attracted to the wall immediately, and the liquid became transparent within 60 to 180 sec (Fig. 1 b(inset)). The MCP showed a magnetic susceptibility (M_s; emu g^{-1}) value of 14.3 emu g^{-1} with coercivity

(H_c) of 0.7 O_e (k Am^{-1}). The plot of M_s against the applied magnetic field (1 Tesla) (

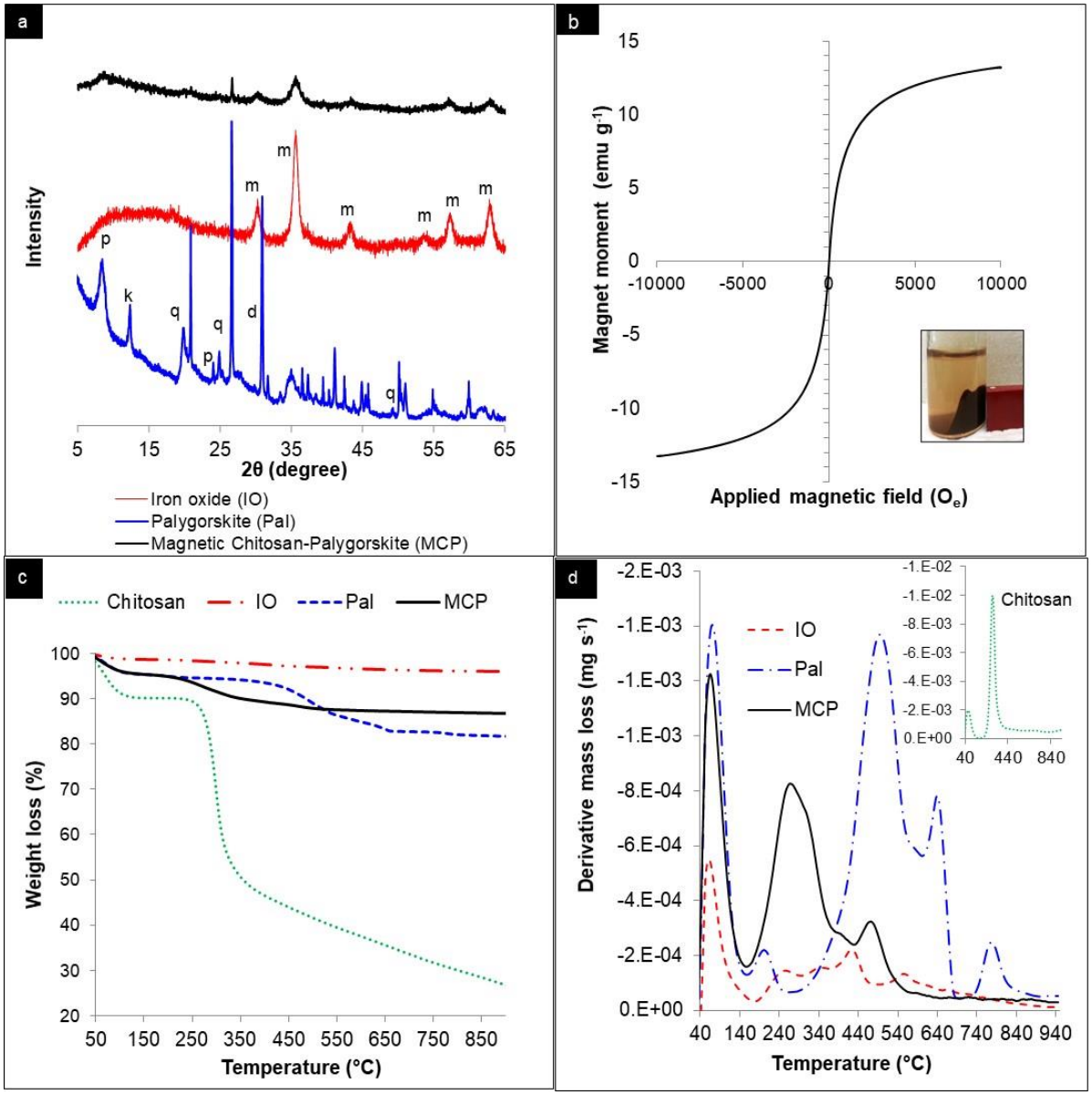

Fig. 1 Fig. 1 b showed a "S" shaped curve with almost no measurable hysteresis loop, which indicated a near-superparamagnetic characteristic of the MCP [23].

In thermogravimetric analysis (TGA), the MCP showed a total weight loss of 13.4% as the temperature was elevated to 950°C. The loss was smaller than the pristine palygorskite (18.5%) and chitosan (75.0%), indicating a higher thermal stability of the nanocomposite (Fig. 1 c). The differential thermogravimetric (DTGA) profile of MCP showed three endothermic weight loss steps (Fig. 1 d; step 1 (4.1% loss with a peak at 68 °C), step 2 (6.4%

loss with a peak at 200 °C), and step 3 (1.6% loss with a peak at 473 °C). Step 1 was assigned to the loss of physisorbed water and some zeolitic water (specifically from palygorskite). The step 2 was responsible for the elimination of the remaining zeolitic water and dehydration of structural water (in palygorskite) combined with a degradation of chitosan macromolecules [24]. A maximum degradation of chitosan was recorded at 390°C, as indicated by the stagnant weight loss (inset in Fig. 1 d). The peak at 635°C (dolomite or calcite decarbonation) and 760°C (dehydroxylation of structural Mg-OH groups observed in palygorskite were undetected in MCP [25], [26], [27]. These findings supported the XRD results that carbonates were removed from the clay mineral during the synthesis of MCP.

MCP had a specific surface area (SSA) of 18.3 $m^2 g^{-1}$, which was lower than the pristine palygorskite (49.4 $m^2 g^{-1}$) (Table 1) due to the macro/nonporous characteristics of chitosan. The MCP exhibited a type IV N_2 adsorption isotherm, which is associated with mesopores ($2 < d < 50$ nm) with the presence of H3 hysteresis loop at P/P_o between 0.4 to 0.9 (SD; Fig. S1 a & b). The zeta potential analysis shows that the palygorskite had a negative surface charge throughout the pH range with no isoelectric point (IEP) displayed, whereas the MCP had an apparent IEP of 4.8 (Fig. S1c). The comparatively positive surface charge of MCP at below pH 5 could be partly contributed by the protonated magnetite nanoparticles (IEP = 5.6) and by chitosan adhered to the surface of MCP (Fig. S1c).

The SEM image revealed that the chitosan layer was mostly present on the outer surface of the MCP nanocomposite, and the palygorskite anchoring the iron oxide nanoparticles constituted the “core” of the nanocomposite (Fig. 2 a). The EDX spectra confirmed the presence of chitosan (ascribed by the N atoms, which represents the amide/amine groups of chitosan), palygorskite (represented by Al and Mg atoms) and magnetite (represented by Fe atoms) (Fig. 2 b). Both bright and dark field STEM images in Figure 2 showed the accumulation of palygorskite and magnetite within the chitosan polymer matrix, and some

298 palygorskite particles were seen projected outside the nanocomposite. It was previously
299 reported that iron oxide (e.g., magnetite) could be encapsulated within the chitosan matrix
300 following their co-precipitation in the presence of a strong base [19], [28]. Similarly,
301 nucleation of Fe^{2+}/Fe^{3+} onto the negative surface of palygorskite during the synthesis was
302 expected. Thus, in the system where both chitosan and palygorskite existed, the Fe^{2+}/Fe^{3+}
303 ions could disperse, nucleate and then grow by forming the crystalline iron oxide
304 nanoparticles on either chitosan, palygorskite, or even at the chitosan-palygorskite interface.
305 The spherical magnetite nanoparticles (particle size in the range of 6 to 40 nm) were
306 distributed regionally in the order of chitosan-palygorskite > palygorskite > chitosan (Fig. 2 c
307 & d). These observations could be associated with the negatively charged surface of
308 palygorskite that provided a greater interaction and stability with iron cations. Thus,
309 palygorskite played a significant role of a structural support for the deposition of magnetite
310 nanoparticles within the nanocomposite. Based on the observation on the surface
311 morphologies of MCP (Fig. 2), the schematic reaction mechanism was proposed, as in Fig. 3
312 a.
313
314 3.2 Advantages of one-pot synthesis of magnetic chitosan-palygorskite
315 The flow diagram of MCP synthesis (Fig. 3 b) showed that the developed one-pot synthesis
316 approach had five main advantages: (i) no pretreatment step (activation) for palygorskite was
317 needed, (ii) co-precipitation of iron oxide (magnetite) could be achieved in-situ, (iii) all
318 components (chitosan, palygorskite and iron oxide) could be simultaneously interacted
319 (electrostatically) in one medium, (iv) precipitation (solidification) of MCP products could be
320 achieved using a common base (i.e., NH_4OH), and (v) the solidified MCP could be separated
321 from the reaction medium using an external magnetic field or simple filtration (Fig. 3 b). The
322 methods applied in this study improves the previous approach in the synthesis of similar

nanocomposites by eliminating the use of potentially hazardous or expensive substances (e.g., organic solvents, surfactants or crosslinkers) and minimized the waste [18], [29]. The synthesis was straight-forward, fast and accomplished under mild experimental conditions (at a temperature range of 25 – 60 °C and atmospheric pressure, no harsh solvent used). The applied method was thus much greener, and could potentially solve the issue of high-cost associated with conventional nanocomposite synthesis methods [19], [28].

3.3 Adsorption studies

3.3.1 Effect of pH and adsorption isotherm

In aqueous systems, Pb ions could exist as mono (Pb^{2+}) or polynuclear species (e.g., $Pb_2(OH)^{3+}$, $Pb_3(OH)^{4+}$) due to the solvation, hydrolysis and polymerisation effect [30]. The hydrolysed Pb^{2+} usually occurs at a higher pH and is prone to precipitation. Hence, the Pb^{2+} adsorption was conducted at a pH range of 3 to 7 to avoid Pb precipitation. The MCP demonstrated a high percentage of Pb^{2+} removal (> 85%; at initial Pb concentration of 50 mg L^{-1}) at all the selected pH values (Fig. S2). Although MCP had IEP of 4.8, the consistent Pb^{2+} removal performance over the entire pH range indicated that the adsorbent's affinity towards Pb^{2+} could not be explained solely based on electrostatic interaction. The pH 4 was used as the working pH in remaining adsorption experiments in this study as this pH recorded the highest Pb^{2+} removal (>99%) (Fig. S2).

The maximum amount of Pb^{2+} adsorption onto MCP obtained in this study was 58.5 mg g^{-1} (Table 2). The adsorption isotherm data were well fitted to the Langmuir model ($R^2 = 0.98$ at $p < 0.05$) (Table 2), suggesting a monolayer adsorption on homogeneous adsorbent surface (MCP). The high adsorption capacity was most likely due to the synergic interplay of various functional groups (e.g., $-NH_2$, $Si-O^-$, FeO^-, OH) contained in the MCP that enhanced the nanocomposite's affinity towards Pb^{2+}. Meanwhile, the *E* value calculated from the D-R

348 model was 12.9 kJ mol^{-1} (Table 2), which indicated that the adsorption was a chemisorption
349 mechanism (*E* value between 8 to 16 kJ mol^{-1}) [31].
350
351 *3.3.2 Adsorption kinetics*
352 The adsorption kinetic data were best fitted to the intra-particle diffusion model (R^2 = 0.96, at
353 $p < 0.05$) among all the kinetic models tested (Table 3; Fig. 4 a). This could be attributed to
354 the chitosan coating on the outer layer of MCP that significantly influenced the diffusion of
355 the adsorbate (Pb^{2+}) [32]. Hence, the adsorption of Pb^{2+} on the active sites of MCP external
356 surfaces was likely followed by a diffusion process into the pores of the nanocomposite.
357 Since the intra-particle diffusion plot did not cross the origin of diffusion (Fig. 4.Fig. 4 a),
358 film diffusion might have played a key role as the rate-determining step for Pb^{2+} adsorption
359 on MCP [33].
360 The intra-particle diffusion plot could be divided into three linear stages (Fig. 4 a). Stage 1
361 was assigned for the film diffusion experienced during the fast transportation of the adsorbate
362 (Pb^{2+}) from bulk solution towards the external surface of MCP [34]. The gradual increase in
363 adsorption (stage 2) and attainment of equilibrium (stage 3) were likely due to the pore (or
364 particle) diffusion processes. By applying the intra- particle diffusion equation at each stage,
365 the slope and intercept might represent the k_i (diffusion rate) and film thickness, respectively
366 (Fig. 4 a). The greater the slope, the faster is the adsorption process [35]. The k_i parameter at
367 each stage showed that the film diffusion (stage 1) was a slower process than the pore (or
368 particle) diffusion (stage 2 and 3) (Fig. 4 a). Accordingly, the intercept values were reduced
369 dramatically (from 7.09 at stage 1 to 0.929 at stage 3) which indicated a decrease in the
370 boundary layer thickness (Fig. 4 a) [35]. The thickness value is usually correlated with the
371 degree of mass transfer resistance; the thicker the boundary, the higher the resistance. Hence,
372 the initial diffusion stage (stage 1) experienced the highest mass transfer resistance effect

(Fig. 4 a), most likely due to the chitosan coating deposited on the external surface [36]. This observation suggested that Pb^{2+} solute first interacted with active sites of chitosan (NH_2 and OH) on the external surface of MCP. When the external surface was almost occupied, the solute travelled through the chitosan polymeric network to reach into internal pores of palygorskite and magnetite. As mentioned above, the diffusion rate at stage 2 (0.9214 mg g^{-1} $min^{0.5}$) and stage 3 (1.2071 mg g^{-1} $min^{0.5}$) were faster than those rate in stage 1 (0.9122 mg g^{-1} $min^{0.5}$) (Fig. 4 a) because the diffusion of Pb^{2+} to mesoporous palygorskite and magnetite was easier than in the tortuous chitosan polymeric network. Furthermore, the rate was faster likely due to the tendency of achieving the equilibrium causing a rapid uptake [4], [37].

To support the diffusion hypothesis, the Boyd model was applied to determine the actual rate determining step, either film (boundary-layer) diffusion or particle diffusion (SD2) [38]. The Boyd model analysis showed that the linear plot did not cross the origin (Fig. 4 b), which confirmed that the external mass transfer by film diffusion was the rate controlling mechanism in the Pb^{2+} adsorption system. Similar results were also reported in previous studies related to polymeric composite in which the kinetic data were well-described by the intra-particle diffusion model [34], [36], [39].

3.3.3 Thermodynamic study

The negative ΔG° values (Table S1) confirmed that the adsorption was spontaneous in nature and energetically favourable [40]. At a similar temperature (e.g., 25°C), the ΔG° became less negative at higher initial Pb^{2+} concentration. These findings suggested that the adsorption process at low solute (Pb^{2+}) concentration was more favourable than at high solute concentration. The concentration gradient created greater driving force to reduce the mass transfer resistance for more collision with the active adsorption sites of MCP. Consequently, some steric effect could possibly present due to aggressive binding competition among Pb^{2+}

crowd towards the active sites. The hindered access towards active sites thus reduced the spontaneity of the reaction. On the other hand, at a similar concentration (e.g., 100 mg L^{-1}) the ΔG° became more negative at high temperature (Table S1), which indicated that the adsorption was more spontaneous with temperature increase. The ΔG° value also signified the type of mechanisms (electrostatic interaction (physisorption), ion-exchange, or charge sharing and/or transfer related to chemisorption) [41]. Physisorption usually shows a small ΔG° value (between -20.0 to 0 kJ mol^{-1}), while chemisorption involves ΔG° in the range of −80 and −400 kJ mol^{-1} [42]. Based on this classification, the adsorption at 50 mg L^{-1} (ΔG° < -100 kJ mol^{-1}) most likely occurred through chemisorption, while some physisorption also took place at a high Pb^{2+} concentration (Table S1).

The positive ΔH° values for all systems indicated that the adsorption was endothermic in nature (Table S1) [43]. The adsorption at 50 and 100 mg L^{-1} Pb^{2+} displayed ΔH° values larger than 40 kJ mol^{-1} (absolute), thus the adsorption mechanism was controlled mainly by chemisorption [43]. Meanwhile, physisorption (ΔH° < 40 kJ mol^{-1}) likely occurred at high Pb^{2+} concentration (200 mg L^{-1}) (Table S1), which signified the occurrence of multilayer adsorption. The positive standard entropy change (ΔS°) (Table S1) signified the increasing randomness at the solid–liquid interface, which might be explained through the concept of desorption of pre-adsorbed water surrounding the MCP interface in an aqueous suspension, as proposed by Barshad [44]. As the Pb^{2+} ions were adsorbed on the active sites, the pre-adsorbed water was displaced to accommodate Pb^{2+}. Thus, the desorbed water molecules from the pre-adsorbed state to a free state increased the randomness in the system [44]. From another perspective, the adsorption of Pb^{2+} on the active sites of MCP made them to be immobilised and static. Hence, the ions on the active sites were more ordered than those in the diffused layer. Thus, the decreased randomness at higher Pb^{2+} concentration was associated with the saturation of active sites by the immobilised Pb^{2+} ions. A similar idea was

proposed in explaining the endothermic nature of Co^{2+} and anionic dye adsorption on kaolinite and coffee waste-derived adsorbent [9], [45].

3.3.4 Adsorption mechanisms revealed through spectroscopic investigations

In the FTIR spectrum of MCP, the -OH stretching band located at 3712 cm^{-1} and 3530 cm^{-1} were the characteristic bands of palygorskite (Fig. 5) [46]. Accordingly, the Al-Al-OH bending, Si-O-Si asymmetric stretching and Si-O-Si bending accounted from the palygorskite were observed at 910, 1030 and 471 cm^{-1}, respectively. Meanwhile, the bands at 563 cm^{-1} and 428 cm^{-1} corresponded to the stretching mode of Fe-O in magnetite (Fe_3O_4) [47], [48], [49]. Chitosan showed a broad band (due to hydrogen bonding) at around 3450 cm^{-1} and a sharp band at 1650 cm^{-1} (Fig. 5). The above band positions were overlapping with the N–H stretching vibration of chitosan (normally occurs at 3417 cm^{-1}), while the N-H bending mode was observed at 3621 cm^{-1}. The C-H stretching vibrations of the chitosan glucosamine ring were present at 2919 and 2860 cm^{-1} [50].

In the Pb^{2+} loaded-MCP (denoted as MCP-Pb) IR spectrum, three regions experienced significant changes (Fig. 5). The first region at around 3700 to 3500 cm^{-1} corresponded to the O-H stretching bands in the clay mineral shifted to a lower wavenumber, which implied an increase of bond length due to changes of electronegativity of neighbouring atoms, for example, via the formation of hydrogen bonds. In the IR spectrum of MCP-Pb, the broad band between 3500 to 3000 cm^{-1} was sharpened likely due to the interaction with Pb^{2+}, indicating a disruption of the internal hydrogen bonds existing within the –OH and N-H groups of chitosan. At the second region (1600 to 1300 cm^{-1}) a more distinguished strong band at 1381 cm^{-1} appeared in MCP-Pb, which was assigned to the bending of long chain aliphatic carbon (-CH_2) of chitosan, C-N stretching band or the –C-OH stretching [51], [52]. A strong band in this region signalled a large change in dipole moment (more polar).

Meanwhile, the band at 563 cm^{-1} in the third region corresponding to the Fe-O stretching vibration of magnetite shifted to a lower wavenumber (539 cm^{-1}) and became weaker, which suggested a possible Pb^{2+} interaction with the oxygen atoms of magnetite nanoparticles [53]. The XPS survey spectrum of MCP showed the presence of Al, Si, Mg (corresponding to palygorskite), N and C (from chitosan), Fe (from magnetite) and O (associated with all these components) (Fig. 6 a). The presence of Pb in Pb-loaded MCP (MCP-Pb) spectrum was confirmed at the binding energy around 137 ($Pb_{4f7/2}$) and 142 eV ($Pb_{4f5/2}$) (Fig. 6 a) [54], [55]. The photoelectron peaks at 137.7 and 136.8 eV (

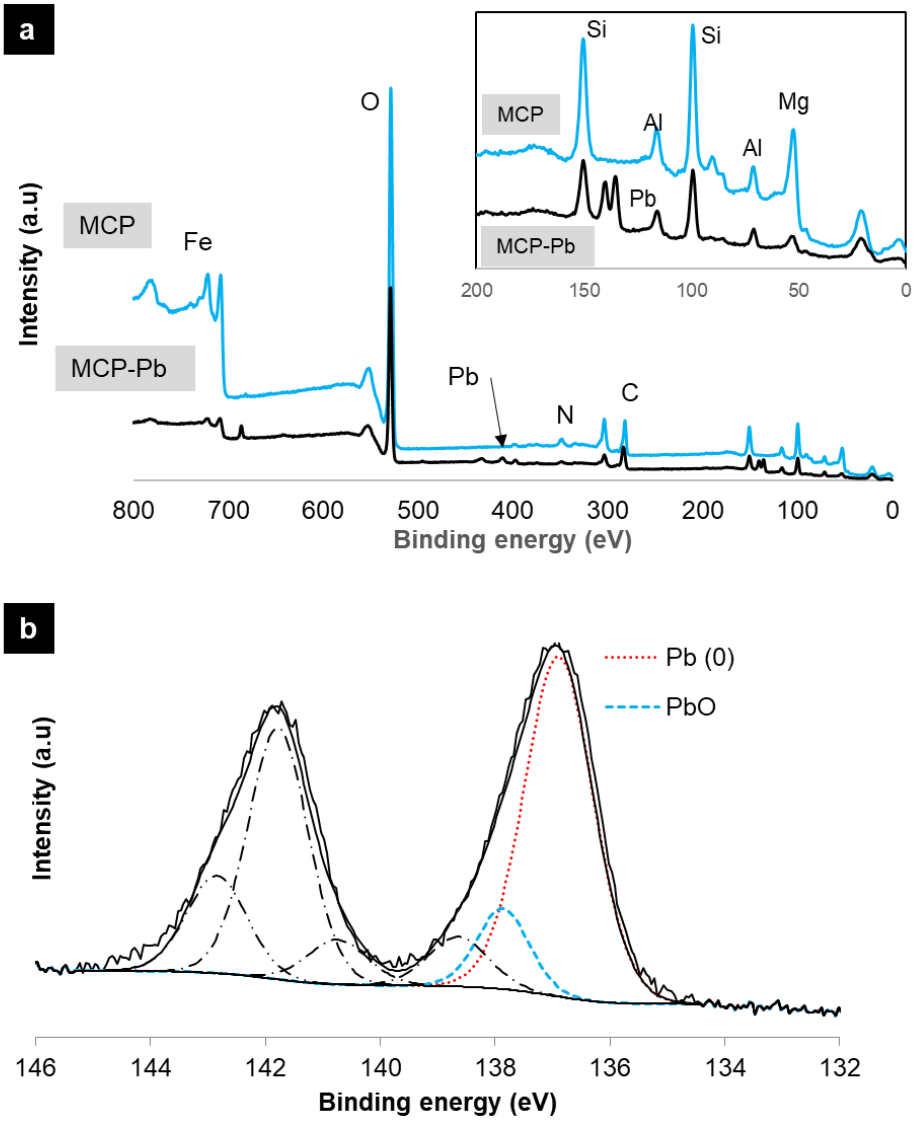

Fig. 6.6 b) corresponded to PbO and zero valent Pb (Pb^0), respectively [56]. The presence of both the Pb species indicated the adsorption and simultaneous reduction mechanisms for Pb^{2+}

459 removal by the MCP, which is reported for the first time in this study compared to previous
460 studies involving similar group of adsorbents.
461 The O_{1S} photoelectron peak at 531.9 eV (Fig. 7 a) corresponded to the hydroxyl groups
462 (- OH) contributed by chitosan, clay mineral, iron oxide, and chemically or physically
463 adsorbed water [57], [58], [59], [60]. The binding energy at 529.8 eV represented the oxygen
464 bonded to Fe (Fe-O species), while the peak at 533.6 was designated to either Si-O or C-O
465 (Fig. 7 a) [61]. In MCP-Pb, a slight shift for the peak at 531.9 (-OH) to 530.3 eV occurred,
466 which suggested the changes of OH chemical environment in the nanocomposite due to Pb
467 adsorption (Fig. 7 b). The shifting of O_{1S} peak towards a lower binding energy region was
468 also observed in previous heavy metal removal studies involving chitosan and iron oxide
469 [59], [60], [61], [62]. In addition, a 55.9% reduction in peak area of Fe-O at 529.8 eV was
470 observed (Fig. 7 b). These findings signified the involvement of OH groups and Fe-O species
471 in the Pb^{2+} removal mechanism, confirming chemisorption. Similarly, Fan et al. showed a
472 shifting of O_{1s} peak to higher binding energy in Pb-loaded palygorskite (thermally treated)
473 [63]. However, the chemical environment of palygorskite assembled in the chitosan-iron
474 oxide matrix (in MCP) in this study was greatly different from the palygorskite only system
475 reported by Fan et al. [63]. Therefore, answering the question why O_{1s} peak shift occurred in
476 palygorskite in MCP requires further investigation.
477 The deconvolution of C_{1s} spectra in MCP (Fig. 7 c) produced four peaks at 284.7, 285.9,
478 287.1 and 288.5 eV, which were assigned for C-C, C-N, C-O and C=O species, respectively
479 [64]. The peak fitting of MCP-Pb showed a new peak at 282.2 eV, which was associated with
480 C-H groups from chitosan (Fig. 7 d) [65]. It was reported that the glucosamine unit (at the
481 end chain of chitosan polymer) could act as the reducing agent through the hydroxyl groups
482 at the position 1 of the glucose ring [66], [67]. The oxidation of this group had probably
483 caused the glucose ring opening, resulting in a more “exposed” carbon on the surface, hence

produced a pronounced peak in MCP-Pb (Fig. 7 d). This organic molecule likely caused the reduction of Pb^{2+} to Pb^{0}.

The N_{1S} photoelectron spectrum of chitosan in MCP was split into two peaks located at 402.4 and 399.6 eV (Fig. 7 e). The former peak could be attributed to NH_3^+, while the later could be attributed to $–NH_2$ species [58], [68]. After Pb^{2+} adsorption, a respective 54.4 % and 11.6% reduction in the peak areas of NH_3^+ and $-NH_2$ in MCP-Pb were observed. In addition, a new peak at 400.7 eV could be attributed to NH_2-Pb bonding that would have compromised 12.5% of the total N_{1S} peak area (Fig. 7 f). It is expected that upon the formation of nitrogen-metal complexes, the nitrogen atom would oxidise due to a decrease in electron density leading to a higher binding energy shift (more than 399 eV) [69], [70]. Therefore, overall changes observed on N_{1s} photoelectron spectra of MCP-Pb reflected the participation of nitrogen species of chitosan towards Pb^{2+} removal.

The photoelectron peaks around 722 and 708 eV were associated with the $Fe_{2p1/2}$ and $Fe_{2p3/2}$, respectively (

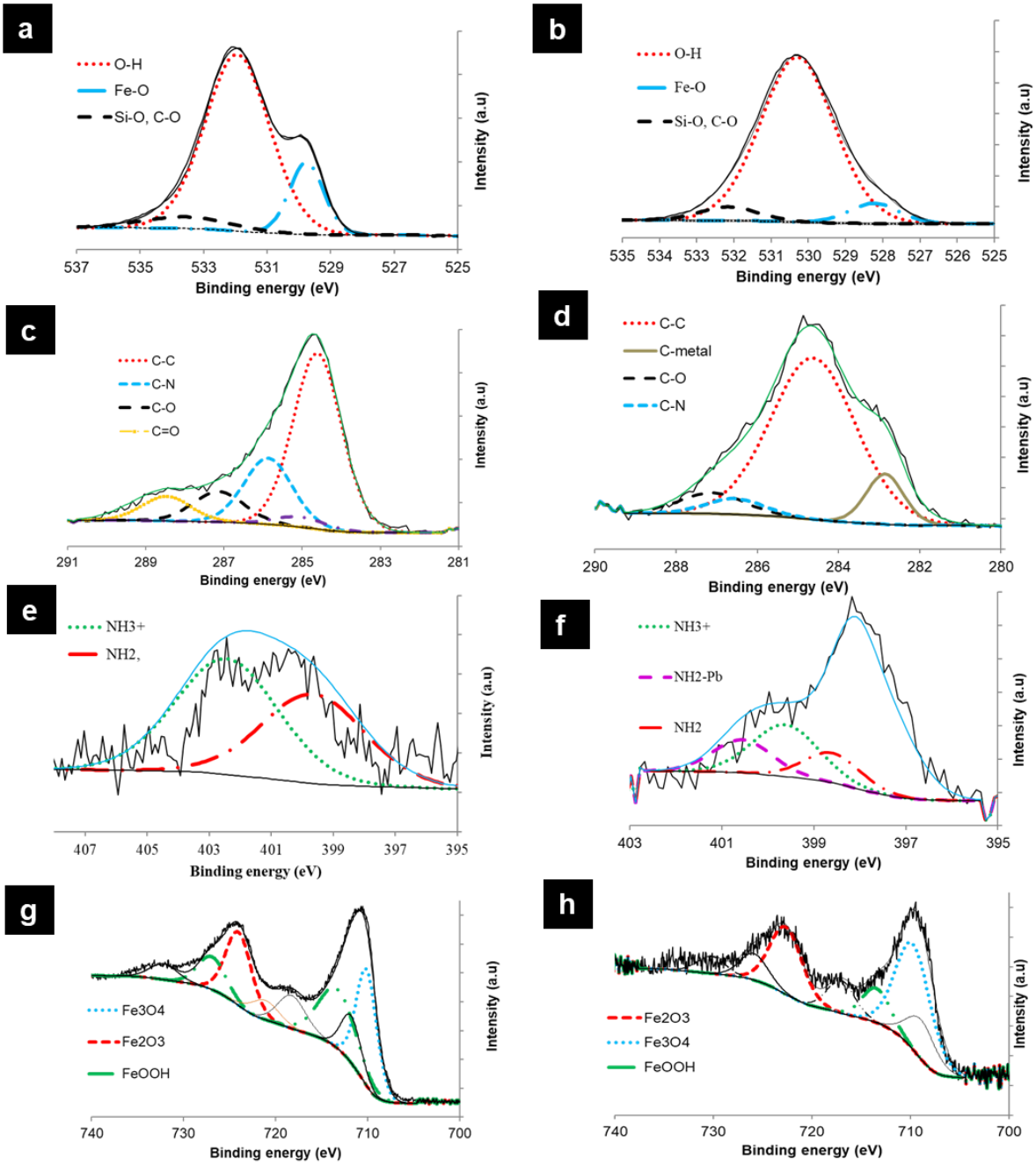

Fig. 7 g). The presence of Fe_3O_4 species was indicated by the photoelectron peak at 710.1 eV (Fig. 7 g) [71]. No significant peak shift was observed for Fe_{2P} in MCP-Pb, nevertheless a higher peak area for Fe_3O_4 (39.5% increase) and a new peak at 708.5 eV (due to Fe_2O_3) were identified (Fig. 7 h) [56]. These observations were probably due to the oxidation of FeO to Fe_2O_3 and/or Fe_3O_4, which happened on the surface of the iron oxide. As the standard reduction potential (E°) of the half-cell equation $Pb^{2+}_{aq} + 2e^- \rightarrow Pb^0$ (-0.13 V) was more

505 positive than the solid state oxidation potential for converting structural Fe_s^{2+} to Fe_s^{3+} (-0.65 to
506 -0.34 V), a spontaneous heterogeneous redox reaction was expected to take place [72]. The
507 reduction of Pb^{2+} to Pb^0 was therefore possible by the resultant electron flow on the
508 magnetite surfaces [72], [73].
509 On the basis of the above data, the removal of Pb by MCP via adsorption and reduction
510 mechanisms could be postulated in a sequence of chemical reactions (Eq. 4 to 9). For Pb^{2+}
511 adsorption, the surface complexation of Pb with the functional hydroxyl groups leads to a
512 decrease in pH, as described in Eq. 4 and 5, respectively:

513 $$\equiv x - OH + Pb^{2+} \leftrightarrow \equiv x\text{-}O\text{-}Pb^{+} + H^{+} \quad \text{(Eq. 4)}$$

514 $$2(\equiv x - OH) + Pb^{2+} \leftrightarrow (\equiv x\text{-}O)_2\text{-}Pb^{0} + 2H^{+} \quad \text{(Eq. 5)}$$

515 where, ≡ x- represents the active surface sites of MCP.
516 The surface complexation through the amine groups of chitosan could be proposed via the
517 following mechanisms (Eq. 6 to 8) [69], [73]:

518 $$\equiv x - NH_3^{+} + Pb^{2+} \rightarrow \equiv x - NH_2Pb^{2+} + H^{+} \quad \text{(Eq. 6)}$$

519 $$\equiv x - NH_2 + Pb^{2+} \rightarrow \equiv x\text{-}NH_2Pb^{2+} \quad \text{(Eq. 7)}$$

520 $$\equiv x - NH_2Pb^{2+} + H_2O \leftrightarrow PbOH^{+} + \equiv x - NH_3^{+} \quad \text{(Eq. 8)}$$

521 The reduction of Pb^{2+} to Pb^0 could be catalysed by the oxidation of Fe^{2+} on the magnetite
522 surface, as proposed by the following nett cell equation (Eq. 9):

523 $$2(\equiv x - Fe_s^{2+}) + \equiv x - Pb^{2+} \rightarrow 2(\equiv x - Fe_s^{3+}) + \equiv x\text{-}Pb^{0} \quad \text{(Eq. 9)}$$

524 The idea of metal reduction phenomena by chitosan is relatively new. Previous studies
525 suggested that the reducing ends (functional groups) of chitosan might get oxidised under
526 acidic working solution (pH 4) and consequently undertake metal reduction, as proposed in
527 studies involving chromate decontamination [74], [75], [76].
528

529 3.4 Adsorbent regeneration study

530 Four Pb^{2+} adsorption-desorption cycles on MCP using 0.01 M EDTA were successfully
531 conducted where the final adsorption test recorded 82% Pb^{2+} removal from an initial 100 mg
532 L^{-1} adsorbate concentration (Fig. 8(a)). The Pb^{2+} desorption percentage decreased to 70% in
533 the fourth cycle. The TEM image of fresh and spent MCP (after four cycles) (Fig. 8 b & c)
534 showed the changes in the cohesion between chitosan layers and palygorskite/magnetite
535 particles. The magnetite and palygorskite particles were distributed more randomly in the
536 spent MCP than the fresh adsorbent. Nevertheless, the magnetite nanoparticles remained
537 intact in the chitosan-palygorskite network, suggesting the polymer coating would have
538 helped to prevent the leaching of iron from the nanocomposite. No significant dry weight loss
539 of spent MCP was recorded in the final regeneration cycle, and the magnetic susceptibility of
540 MCP was still preserved (M_s = 18.7 emu g^{-1}). These findings confirmed the stability of the
541 nanocomposite in enduring multiple regeneration cycles without significantly losing the
542 adsorption capacity [77].
543

544 3.5 Comparison with other magnetic nanocomposites

545 The above characterisation and adsorption results provided strong evidence for the potential
546 use of MCP as an efficient adsorbent to remove Pb^{2+} from water. To validate the MCP's
547 performance, a comparison with other magnetic nanocomposites used for removing Pb^{2+} was
548 conducted (Table 4). The MCP showed a good performance in terms of maximum adsorption
549 capacity considering the wide initial Pb^{2+} concentration range, low adsorbent loading and
550 high performance at acidic pH used in experiments (Table 4). Nevertheless, the magnetic
551 susceptibility of MCP was relatively low compared to other magnetic adsorbents, which
552 gives an opportunity for further research development in this area.
553

4. Conclusions

A novel one-pot synthesis of magnetic chitosan-palygorskite (MCP) nanocomposite was achieved in this study avoiding the typical steps of clay pre-purification and without using any organic solvent, which otherwise were routinely needed in previously reported nanocomposite synthesis procedures. A suite of state-of-the-art characterization techniques provided evidences for the synergic roles of each component (polymeric chitosan, fibrous palygorskite and nanosized iron oxides) of the nanocomposite either as a structural reinforcement or reactivity enhancer towards Pb^{2+}. The palygorskite acted as an outstanding support for the nucleation of iron oxide nanoparticles and simultaneously provided stability to chitosan within the nanocomposite matrix. Hence, this research may escalate scientific interests for investigating palygorskite as a superior choice of clay minerals to prepare polymer-clay nanocomposites alongside other dominating mineral candidates such as montmorillonite, sepiolite and vermiculite that are frequently reported in literature.

The MCP showed a considerable Pb^{2+} adsorption capacity (58.5 mg g^{-1}), occurring primarily via surface complexation and chemical reduction mechanisms, as revealed via fitting of the experimental adsorption data to fundamental isotherm, kinetic and thermodynamic models coupled with authentication through detailed spectroscopic and magnetic susceptibility analyses. The above approach could be employed to unravel removal mechanisms of aquatic contaminants using a range of adsorbents, and hence deciding the adsorbent's effective performance life and suitable disposal pathway following usage. Moreover, the Pb^{2+} removal performance of the MCP remained almost unaffected up to four adsorption-desorption cycles (using 0.01 M EDTA) with negligible loss of the adsorbent's magnetic susceptibility, which would help to mitigate uncertainties around the durability of magnetic adsorbents for water treatment in future studies.

Overall, this study provides a novel green approach for the preparation of magnetic nanocomposites using natural clay minerals and biowastes (chitosan) for potential applications in environmental heavy metal remediation. Future investigations are needed to further improve the magnetic susceptibility of the nanocomposite, assess its performance of heavy metal removal from real wastewater, and evaluate the nanocomposite's ecotoxicological impacts, if any.

Acknowledgements

Ruhaida Rusmin acknowledges the Ministry of Higher Education of Malaysia and Universiti Teknologi MARA (UiTM) for awarding her a PhD scholarship to pursue this study at University of South Australia, and also acknowledges the partial support from the UiTM Young Talent Researcher Grant (Grant File Number: 600-RMC/YTR/5/3 (006/2020) and Clay Minerals Society (CMS) Student Research Grant. All authors express their gratitude to Dr. Xiang Zhao for assistance in VSM measurement, Dr. Nobuyuki Kawashima for TEM analysis, Mr. Stuart McClure for SEM imaging, Mr. Chris Bassell for XPS data collection, Ms. Susie Ritch for ICP analysis, and Dr. Dario Arrua for supervisory support to Ruhaida Rusmin.

596 **References**

597 [1] M. A. Elias, T. Hadibarata, P. Sathishkumar, Modified oil palm industry solid waste as a
598 potential adsorbent for lead removal, Environ. Chem. Ecotoxicol. 3 (2021) 1-7.
599 https://doi.org/10.1016/j.enceco.2020.10.003

600 [2] L. Meng, Z. Li, L. Liu, X. Chen, J. Wu, W. Li, X. Zhang, M. Dong, Lead removal from
601 water by a newly isolated Geotrichum candidum LG-8 from Tibet kefir milk and its
602 mechanism, Chemosphere. 259 (2020) 127507. doi:10.1016/j.chemosphere.2020.127507.
603 [3] USEPA, National primary drinking water standards, maximum contaminant level, United
604 States Environmental Protection Agency Office of Water, Washington D.C., USA, 2013.
605 [4] R. Rusmin, B. Sarkar, Y. Liu, S. McClure, R. Naidu, Structural evolution of chitosan–
606 palygorskite composites and removal of aqueous lead by composite beads, Appl. Surf. Sci. 353
607 (2015) 363-375.
608 [5] B. Sarkar, R. Rusmin, U.C. Ugochukwu, R. Mukhopadhyay, K.M. Manjaiah, Chapter 5 -
609 Modified clay minerals for environmental applications, in: M. Mercurio, B. Sarkar, A. Langella
610 (Eds.) Modified Clay and Zeolite Nanocomposite Materials, Elsevier, 2019, pp. 113-127.
611 [6] R. Rusmin, B. Sarkar, B. Biswas, J. Churchman, Y. Liu, R. Naidu, Structural, electrokinetic
612 and surface properties of activated palygorskite for environmental application, Appl. Clay
613 Sci.134 (2016) 95-102.

614 [7] Z. Wang, Y. Jiang, X. Mo, X. Gu, W. Li, Speciation transformation of Pb during
615 palygorskite sorption-calcination process: Implications for Pb sequestration, Appl. Geochem.
616 124 (2021) 104850.
617 [8] E. Ruiz-Hitzky, M. Darder, A.C.S. Alcântara, B. Wicklein, P. Aranda, CHAPTER 1
618 Functional Nanocomposites Based on Fibrous Clays, Functional Polymer Composites with
619 Nanoclays, The Royal Society of Chemistry 2017, pp. 1-53.

620 [9] K. G. Bhattacharyya, S.S. Gupta, Adsorption of a few heavy metals on natural and modified
621 kaolinite and montmorillonite: A review, Adv. Colloid Interface Sci. 140 (2008) 114-131.

622 [10] E. I. Unuabonah, C. G. Ugwuja, M. O. Omorogie, A. Adewuyi, N. A. Oladoja, Clays for
623 efficient disinfection of bacteria in water, Appl. Clay Sci. 151 (2018) 211-223.

624 [11] R. Mukhopadhyay, D. Bhaduri, B. Sarkar, R. Rusmin, D. Hou, R. Khanam, S. Sarkar, J.
625 Kumar Biswas, M. Vithanage, A. Bhatnagar, Y.S. Ok, Clay–polymer nanocomposites:
626 Progress and challenges for use in sustainable water treatment, J. Hazard. Mater. 383 (2020)
627 121125.

628 [12] R. Mukhopadhyay, B. Sarkar, E. Khan, D.S. Alessi, J.K. Biswas, K.M. Manjaiah, M.
629 Eguchi, K.C.W. Wu, Y. Yamauchi, Y.S. Ok, Nanomaterials for sustainable remediation of
630 chemical contaminants in water and soil, Crit. Rev. Environ. Sci. Technol. (2021) 1-50.

631 [13] G. Feng, J. Ma, X. Zhang, Q. Zhang, Y. Xiao, Q. Ma, S. Wang, Magnetic natural
632 composite Fe_3O_4-chitosan@bentonite for removal of heavy metals from acid mine drainage, J.
633 Colloid Interface Sci. 538 (2019) 132-141.

634 [14] T. Zhang, W. Wang, Y. Zhao, H. Bai, T. Wen, S. Kang, G. Song, S. Song, S. Komarneni,
635 Removal of heavy metals and dyes by clay-based adsorbents: From natural clays to 1D and 2D
636 nano-composites, Chem. Eng. J. (2020) 127574.

637 [15] S. Begum, N.Y. Yuhana, N. Md Saleh, N.H.N. Kamarudin, A.B. Sulong, Review of
638 chitosan composite as a heavy metal adsorbent: Material preparation and properties,
639 Carbohydr. Polym. 259 (2021) 117613.

640 [16] D.-W. Cho, B.-H. Jeon, C.-M. Chon, F.W. Schwartz, Y. Jeong, H. Song, Magnetic
641 chitosan composite for adsorption of cationic and anionic dyes in aqueous solution, J. Ind. Eng.
642 Chem. 28 (2015) 60-66.

643 [17] A. Bée, L. Obeid, R. Mbolantenaina, M. Welschbillig, D. Talbot, Magnetic chitosan/clay
644 beads: A magsorbent for the removal of cationic dye from water, J. Magn. Magn. Mater. 421
645 (2017) 59-64.

646 [18] V. Arya, L. Philip, Adsorption of pharmaceuticals in water using Fe_3O_4 coated polymer
647 clay composite, Microporous Mesoporous Mater. 232 (2016) 273-280.

648 [19] M.M. Sobeih, M.F. El-Shahat, A. Osman, M.A. Zaid, M.Y. Nassar, Glauconite clay-
649 functionalized chitosan nanocomposites for efficient adsorptive removal of fluoride ions from
650 polluted aqueous solutions, RSC Adv. 10 (2020) 25567-25585.

651 [20] B. Sarkar, E. Liu, S. McClure, J. Sundaramurthy, M. Srinivasan, R. Naidu, Biomass
652 derived palygorskite–carbon nanocomposites: Synthesis, characterisation and affinity to dye
653 compounds, Appl. Clay Sci. 114 (2015) 617-626

654 [21] J. Chen, L.-g. Yan, H.-q. Yu, S. Li, L.-l. Qin, G.-q. Liu, Y.-f. Li, B. Du, Efficient removal
655 of phosphate by facile prepared magnetic diatomite and illite clay from aqueous solution,
656 Chem. Eng. J. 287 (2016) 162-172.
657 [22] Y. Yahia, F. García-Villén, A. Djelad, L.S. Belaroui, R. Sanchez-Espejo, M. Sassi, A.
658 López-Galindo, C. Viseras, Crosslinked palygorskite-chitosan beads as diclofenac carriers,
659 Appl. Clay Sci. 180 (2019) 105169.
660 [23] R. Rusmin, B. Sarkar, T. Tsuzuki, N. Kawashima, R. Naidu, Removal of lead from
661 aqueous solution using superparamagnetic palygorskite nanocomposite: Material
662 characterization and regeneration studies, Chemosphere. 186 (2017) 1006–1015.

663 [24] E. P. Jeffrey, J. H. Peter, Synchrotron powder X-ray diffraction study of the structure and
664 dehydration behavior of palygorskite, Am. Mineral. 93 (2008) 667-675.

665 [25] S. Guggenheim, A. F. K. V. Groos, Baseline studies of the Clay Minerals Society source
666 clays: Thermal analysis, Clays Clay Miner. 49 (2001), 433-443.

667 [26] H. Cheng, J. Yang, R.L. Frost, Thermogravimetric analysis-mass spectrometry (TG-MS)
668 of selected Chinese palygorskites—Implications for structural water, Thermochim. Acta. 512
669 (2011) 202-207.

670 [27] R.L. Frost, Z. Ding, Controlled rate thermal analysis and differential scanning calorimetry
671 of sepiolites and palygorskites, Thermochim. Acta. 397 (2003) 119-128.

672 [28] D. H. K. Reddy, S. –M. Lee, Application of magnetic chitosan composites for the removal
673 of toxic metal and dyes from aqueous solutions, Adv. Colloid Interface Sci. 201–202 (2013),
674 68-93.

675 [29] T. Aydemir, S. Güler, Characterization and immobilization of Trametes versicolor laccase
676 on magnetic chitosan–clay composite beads for phenol removal, Artif Cells Nanomed
677 Biotechnol. 43 (2015) 425-432.

678 [30] J. Wang, S. Xia, L. Yu, Adsorption of Pb(II) on the kaolinite(001) surface in aqueous
679 system: A DFT approach, Appl. Surf. Sci. 339 (2015) 28-35

680 [31] B. Sarkar, Y. Xi, M. Megharaj, G.S.R. Krishnamurti, R. Naidu, Synthesis and
681 characterisation of novel organopalygorskites for removal of p-nitrophenol from aqueous
682 solution: Isothermal studies, J. Colloid Interface Sci. 350 (2010) 295-304.
683 [32] E.O. Oyelude, J.A.M. Awudza, S.K. Twumasi, Equilibrium, Kinetic and Thermodynamic
684 Study of Removal of Eosin Yellow from Aqueous Solution Using Teak Leaf Litter Powder,
685 Sci. Rep. 7 (2017) 12198.

686 [33] M.S. Podder, C.B. Majumder, Biosorption of As(III) and As(V) on the surface of
687 TW/$MnFe_2O_4$ composite from wastewater: kinetics, mechanistic and thermodynamics, Appl.
688 Water Sci. 7 (2017) 2689-2715.
689 [34] Y. Chen, J. Wang, Removal of radionuclide Sr^{2+} ions from aqueous solution using
690 synthesized magnetic chitosan beads, Nucl. Eng. Des. 242 (2012) 445–451.
691 [35] A. Pholosi, E.B. Naidoo, A.E. Ofomaja, Intraparticle diffusion of Cr(VI) through biomass
692 and magnetite coated biomass: A comparative kinetic and diffusion study, S. Afr. J. Chem.
693 Eng. 32 (2020) 39-55.
694 [36] S. –Y. Pan, W. –J. Syu, T. –K. Chang, C. –H. Lee, A multiple model approach for
695 evaluating the performance of time-lapse capsules in trapping heavy metals from water bodies,
696 RSC Adv. 10(2020), 16490–16501.

697 [37] W. H. Cheung, Y. S. Szeto, G. McKay, Intraparticle diffusion processes during acid dye
698 adsorption onto chitosan, Bioresour. Technol. 98 (2007) 2897-2904.

699 [38] G.E. Boyd, A.W. Adamson, L.S. Myers, The Exchange Adsorption of Ions from Aqueous
700 Solutions by Organic Zeolites. II. Kinetics1, J. Am. Chem. Soc. 69 (1947) 2836-2848.
701 [39] S. I. Siddiqui, P. N. Singh, N. Tara, S. Pal, S. A. Chaudhry, I. Sinha, Arsenic removal from
702 water by starch functionalized maghemite nano-adsorbents: Thermodynamics and kinetics
703 investigations, Colloid Interface Sci. Commun. 36 (2020) 100263.

704 [40] H.N. Tran, S.-J. You, H.-P. Chao, Thermodynamic parameters of cadmium adsorption
705 onto orange peel calculated from various methods: A comparison study, J. Environ. Chem.
706 Eng. 4 (2016) 2671-2682.
707 [41] Y. Liu, Is the Free Energy Change of Adsorption Correctly Calculated?, J. Chem. Eng.
708 Data. 54 (2009) 1981-1985.

709 [42] A.N. Fernandes, C.A.P. Almeida, N.A. Debacher, M.M.d.S. Sierra, Isotherm and
710 thermodynamic data of adsorption of methylene blue from aqueous solution onto peat, J. Mol.
711 Struct. 982 (2010) 62-65.
712 [43] K. Rasoulpoor, A. Poursattar Marjani, E. Nozad, Competitive chemisorption and
713 physisorption processes of a walnut shell based semi-IPN bio-composite adsorbent for lead ion
714 removal from water: Equilibrium, Kinetic and Thermodynamic studies, Environ. Technol.
715 Innov. 20 (2020) 101133.
716 [44] I. Barshad, Thermodynamics of Water Adsorption and Desorption on Montmorillonite,
717 Clays Clay Miner. 8 (1959) 84-101.
718 [45] S. Wong, N.A. Ghafar, N. Ngadi, F.A. Razmi, I.M. Inuwa, R. Mat, N.A.S. Amin, Effective
719 removal of anionic textile dyes using adsorbent synthesized from coffee waste, Sci. Rep. 10
720 (2020) 2928.
721 [46] M. Suárez, E. García-Romero, FTIR spectroscopic study of palygorskite: Influence of the
722 composition of the octahedral sheet, Appl. Clay Sci. 31 (2006) 154-163.
723 [47] J. Madejová, P. Komadel, Baseline studies of the clay minerals society source clays:
724 Infrared methods, Clays Clay Miner. 49 (2001) 410-432.
725 [48] H. Namduri, S. Nasrazadani, Quantitative analysis of iron oxides using Fourier transform
726 infrared spectrophotometry, Corros. Sci. 50 (2008) 2493-2497.
727 [49] R. Mukhopadhyay, T. Adhikari, B. Sarkar, A. Barman, R. Paul, A.K. Patra, P.C. Sharma,
728 P. Kumar, Fe-exchanged nano-bentonite outperforms Fe_3O_4 nanoparticles in removing nitrate
729 and bicarbonate from wastewater, J. Hazard. Mater. 376 (2019) 141-152.
730 [50] D.-W. Cho, B.-H. Jeon, C.-M. Chon, Y. Kim, F.W. Schwartz, E.-S. Lee, H. Song, A novel
731 chitosan/clay/magnetite composite for adsorption of Cu(II) and As(V), Chem. Eng. J. 200-202
732 (2012) 654-662.

733 [51] Y. Wen, C. Shen, Y. Ni, S. Tong, F. Yu, Glow discharge plasma in water: A green
734 approach to enhancing ability of chitosan for dye removal, J. Hazard. Mater. 201-202 (2012)
735 162-169.
736 [52] L. Fan, C. Luo, X. Li, F. Lu, H. Qiu, M. Sun, Fabrication of novel magnetic chitosan
737 grafted with graphene oxide to enhance adsorption properties for methyl blue, J. Hazard. Mater.
738 215-216 (2012) 272-279.
739 [53] M. Mohapatra, K. Rout, B.K. Mohapatra, S. Anand, Sorption behavior of Pb(II) and Cd(II)
740 on iron ore slime and characterization of metal ion loaded sorbent, J. Hazard. Mater. 166 (2009)
741 1506-1513.

742 [54] J. F. Moulder, W. F. Stickle, P. E. Sobol, K. D. Bomben, Handbook of X-ray Photoelectron
743 Spectroscopy, Perkin-Elmer Corporation (Physical Electronics Division) 1992. United States
744 of America.

745 [55] X. Zhang, S. Lin, Z. Chen, M. Megharaj, R. Naidu, Kaolinite-supported nanoscale zero-
746 valent iron for removal of Pb^{2+} from aqueous solution: Reactivity, characterization and
747 mechanism, Water Res. 45 (2011) 3481-3488.
748 [56] Y. Xi, M. Mallavarapu, R. Naidu, Reduction and adsorption of Pb^{2+} in aqueous solution
749 by nano-zero-valent iron—A SEM, TEM and XPS study, Bull. Mar. Sci. 45 (2010) 1361-1367.

750 [57] X. –Q. Li, W. –X. Zhang, Sequestration of metal cations with zerovalent iron
751 nanoparticlesa study with High Resolution X-ray Photoelectron Spectroscopy (HR-XPS), J.
752 Phys. Chem. C. 111 (2007) 6939-6946.

753 [58] C. Shen, Y. Shen, Y. Wen, H. Wang, W. Liu, Fast and highly efficient removal of dyes
754 under alkaline conditions using magnetic chitosan-Fe(III) hydrogel, Water Res. 45 (2011)
755 5200-5210.

[59] C.-Y. Cao, J. Qu, W.-S. Yan, J.-F. Zhu, Z.-Y. Wu, W.-G. Song, Low-Cost Synthesis of Flowerlike α-Fe2O3 Nanostructures for Heavy Metal Ion Removal: Adsorption Property and Mechanism, Langmuir. 28 (2012) 4573-4579.

[60] P. Krishnan, M. Liu, P.A. Itty, Z. Liu, V. Rheinheimer, M.-H. Zhang, P.J.M. Monteiro, L.E. Yu, Characterization of photocatalytic TiO_2 powder under varied environments using near ambient pressure X-ray photoelectron spectroscopy, Sci. Rep. 7 (2017) 43298.

[61] N.A. Travlou, G.Z. Kyzas, N.K. Lazaridis, E.A. Deliyanni, Functionalization of Graphite Oxide with Magnetic Chitosan for the Preparation of a Nanocomposite Dye Adsorbent, Langmuir. 29 (2013) 1657-1668.

[62] L. Zhao, H. Mitomo, Adsorption of heavy metal ions from aqueous solution onto chitosan entrapped CM-cellulose hydrogels synthesized by irradiation, J. Appl. Polym. Sci. 110 (2008) 1388-1395.

[63] Q. Fan, Z. Li, H. Zhao, Z. Jia, J. Xu, W. Wu, Adsorption of Pb(II) on palygorskite from aqueous solution: Effects of pH, ionic strength and temperature, Appl. Clay Sci. 45 (2009) 111-116.

[64] R.S. Vieira, M.L.M. Oliveira, E. Guibal, E. Rodríguez-Castellón, M.M. Beppu, Copper, mercury and chromium adsorption on natural and crosslinked chitosan films: An XPS investigation of mechanism, Colloids Surf, A Physicochem Eng Asp. 374 (2011) 108-114.

[65] M. Wang, Y. She, Z. Xiao, J. Hu, R. Zhou, J. Zhang, The green adsorption of chitosan tripolyphosphate nanoparticles on cotton fiber surfaces, Carbohydr. Polym. 101 (2014) 812-818.

[66] H. Huang, X. Yang, Synthesis of Chitosan-Stabilized Gold Nanoparticles in the Absence/Presence of Tripolyphosphate, Biomacromolecules. 5 (2004) 2340-2346.

[67] Y.-J. Jiang, X.-Y. Yu, T. Luo, Y. Jia, J.-H. Liu, X.-J. Huang, γ-Fe_2O_3 Nanoparticles Encapsulated Millimeter-Sized Magnetic Chitosan Beads for Removal of Cr(VI) from Water:

781 Thermodynamics, Kinetics, Regeneration, and Uptake Mechanisms, J. Chem. Eng. Data. 58
782 (2013) 3142-3149.
783 [68] L. Dambies, T. Vincent, E. Guibal, Treatment of arsenic-containing solutions using
784 chitosan derivatives: uptake mechanism and sorption performances, Water Res. 36 (2002)
785 3699-3710.
786 [69] L. Jin, R. Bai, Mechanisms of Lead Adsorption on Chitosan/PVA Hydrogel Beads,
787 Langmuir. 18 (2002) 9765-9770.
788 [70] Y. Zhu, J. Hu, J. Wang, Competitive adsorption of Pb(II), Cu(II) and Zn(II) onto xanthate-
789 modified magnetic chitosan, J. Hazard. Mater. 221-222 (2012) 155-161.
790 [71] C. Dong, W. Chen, C. Liu, Y. Liu, H. Liu, Synthesis of magnetic chitosan nanoparticle
791 and its adsorption property for humic acid from aqueous solution, Colloids Surf, A
792 Physicochem Eng Asp. 446 (2014) 179-189.
793 [72] A.F. White, M.L. Peterson, Reduction of aqueous transition metal species on the surfaces
794 of Fe(II) -containing oxides, Geochim. Cosmochim. Acta. 60 (1996) 3799-3814.
795 [73] H.A. Wiatrowski, S. Das, R. Kukkadapu, E.S. Ilton, T. Barkay, N. Yee, Reduction of
796 Hg(II) to Hg(0) by Magnetite, Environ. Sci. Technol. 43 (2009) 5307-5313.
797 [74] L. Dambies, C. Guimon, S. Yiacoumi, E. Guibal, Characterization of metal ion
798 interactions with chitosan by X-ray photoelectron spectroscopy, Colloids Surf, A
799 Physicochem Eng Asp. 177 (2001) 203-214.
800 [75] F.C. de Godoi, E. Rodriguez-Castellon, E. Guibal, M.M. Beppu, An XPS study of
801 chromate and vanadate sorption mechanism by chitosan membrane containing copper
802 nanoparticles, Chem. Eng. J. 234 (2013) 423-429.
803 [76] S. Mandal, B. Sarkar, N. Bolan, Y.S. Ok, R. Naidu, Enhancement of chromate reduction
804 in soils by surface modified biochar, J. Environ. Manage. 186 (2017) 277-284.

[77] M. F. Hamza, A. Fouda, K. Z. Elwakeel, Y. Wei, E. Guibal, N. A. Hamad, Phosphorylation of Guar Gum/Magnetite/Chitosan Nanocomposites for Uranium (VI) Sorption and Antibacterial Applications, Molecules 26 (2021) 1920. https://doi.org/10.3390/molecules26071920.

[78] K. Li, Y. Wang, M. Huang, H. Yan, H. Yang, S. Xiao, A. Li, Preparation of chitosan-graft-polyacrylamide magnetic composite microspheres for enhanced selective removal of mercury ions from water, J. Colloid Interface Sci. 455 (2015) 261-270.

[79] H. V. Tran, L. D. Tran, T. N. Nguyen, Preparation of chitosan/magnetite composite beads and their application for removal of Pb(II) and Ni(II) from aqueous solution, Mater. Sci. Eng. C. 30 (2010) 304-310.

[80] X. Liu, Q. Hu, Z. Fang, X. Zhang, B. Zhang, Magnetic chitosan nanocomposites: a useful recyclable tool for heavy metal ion removal, Langmuir. 25 (2009), 3-8.

[81] L. Fan, C. Luo, M. Sun, X. Li, H. Qiu, Highly selective adsorption of lead ions by water-dispersible magnetic chitosan/graphene oxide composites, Colloids Surf. B. 103 (2013) 523-529.

[82] D. Cheng, X. Dai, L. Chen, Y. Cui, C. Qiang, Q. Sun, J. Dai, Thiol-Yne click synthesis of polyamide-amine dendritic magnetic halloysite nanotubes for the efficient removal of Pb (II), ACS Sustain. Chem. Eng. 8 (2020) 771–781.

[83] C. Irawan, I. F. Nata, C. –K. Lee, Removal of Pb(II) and As(V) using magnetic nanoparticles coated montmorillonite via one-pot solvothermal reaction as adsorbent, J. Environ. Chem. Eng. 7 (2019) 103000.

[84] Q. U. Ain, H. Zhang, M. Yaseen, U. Rasheed, K. Liu, S. Subhan, Z. Tong, Facile fabrication of hydroxyapatite-magnetite-bentonite composite for efficient adsorption of Pb (II), Cd (II), and crystal violet from aqueous solution, J. Clean. Prod. 247 (2020) 119088.

829 [85] M. Fayazi, Facile hydrothermal synthesis of magnetic sepiolite clay for removal of Pb (II)
830 from aqueous solutions, Anal. Bioanal. Chem. Res. 6 (2019) 125-136.
831 [86] I. S. Izman, S. N. A. Baharin, R. Rusmin, Magnetic kaolinite composite for lead removal
832 in aqueous solution, Malays. J. Anal. Sci. 24 (2020), 115-124.
833

834 **Figure legends**

835 Fig. 1. Characteristic features of chitosan, palygorskite (Pal), iron oxide (IO) and magnetic
836 chitosan-palygorskite nanocomposite (MCP): (a) XRD pattern (p = palygorskite, q= quartz, d
837 = dolomite, k = kaolinite, m = magnetite), (b) magnetisation curve of MCP, (c) TGA curves,
838 and (d) DTGA profiles. Inset in Fig. 1(b) is the photo of magnetically separated MCP.

839 Fig. 2. Back scattered SEM image (a), EDX spectra (b), Bright Field (c) and Dark Field (d)
840 STEM images of MCP

841 Fig. 3. Schematic illustration (not to scale) on the proposed reaction mechanism (a) and the
842 flow diagram (b) for the synthesis of MCP

843 Fig. 4. Adsorption kinetics analysis of Pb adsorption by MCP: (a) intra-particle diffusion plot,
844 (b) Boyd plot

845 Fig. 5. FTIR spectra of MCP (before adsorption) and Pb^{2+} loaded-MCP (MCP-Pb) (after
846 adsorption)

847 Fig. 6. XPS spectra of MCP and Pb-loaded MCP (MCP-Pb): (a) survey scan, (b) high
848 resolution scan for Pb_{4f}

849 Fig. 7. High Resolution XPS spectra of MCP and Pb-loaded MCP (MCP-Pb): (a-b) $O_{1s,}$ (c-d)
850 C_{1s}, (e-f) N_{1s}, and (g-h) Fe_{2p}

851 Fig. 8. Adsorption-desorption cycle of MCP: (a) Comparison on Pb^{2+} adsorption and
852 desorption (in percentage) by MCP during four subsequent regeneration cycles (error bars
853 represent the standard error at 95% confidence level, n = 2), (b & c): TEM images of fresh (b)
854 and spent MCP after a four adsorption-desorption cycles (c)

855

856 **Title of tables**

857 Table 1. Specific surface area, pore volume and pore diameter of palygorskite (Pal), iron
858 oxide (IO) and magnetic chitosan-palygorskite nanocomposite (MCP).

859 Table 2. Langmuir, Freundlich, Dubinin–Radushkevich and Temkin model parameters for
860 Pb^{2+} adsorption by magnetic chitosan-palygorskite nanocomposite (MCP) ($p < 0.05$, n = 2).

861 Table 3. Adsorption kinetic model parameters of Pb^{2+} adsorption by MCP (initial Pb^{2+}
862 concentration = 200 mg L^{-1}, at 25°C, under 150 agitation per min with 5 g L^{-1} adsorbent
863 loading) at $p < 0.05$, n =2.

864 Table 4. Comparison of the efficiency of Pb^{2+} adsorption by magnetic composites based on
865 important experimental parameters.

866

867 **Figures**

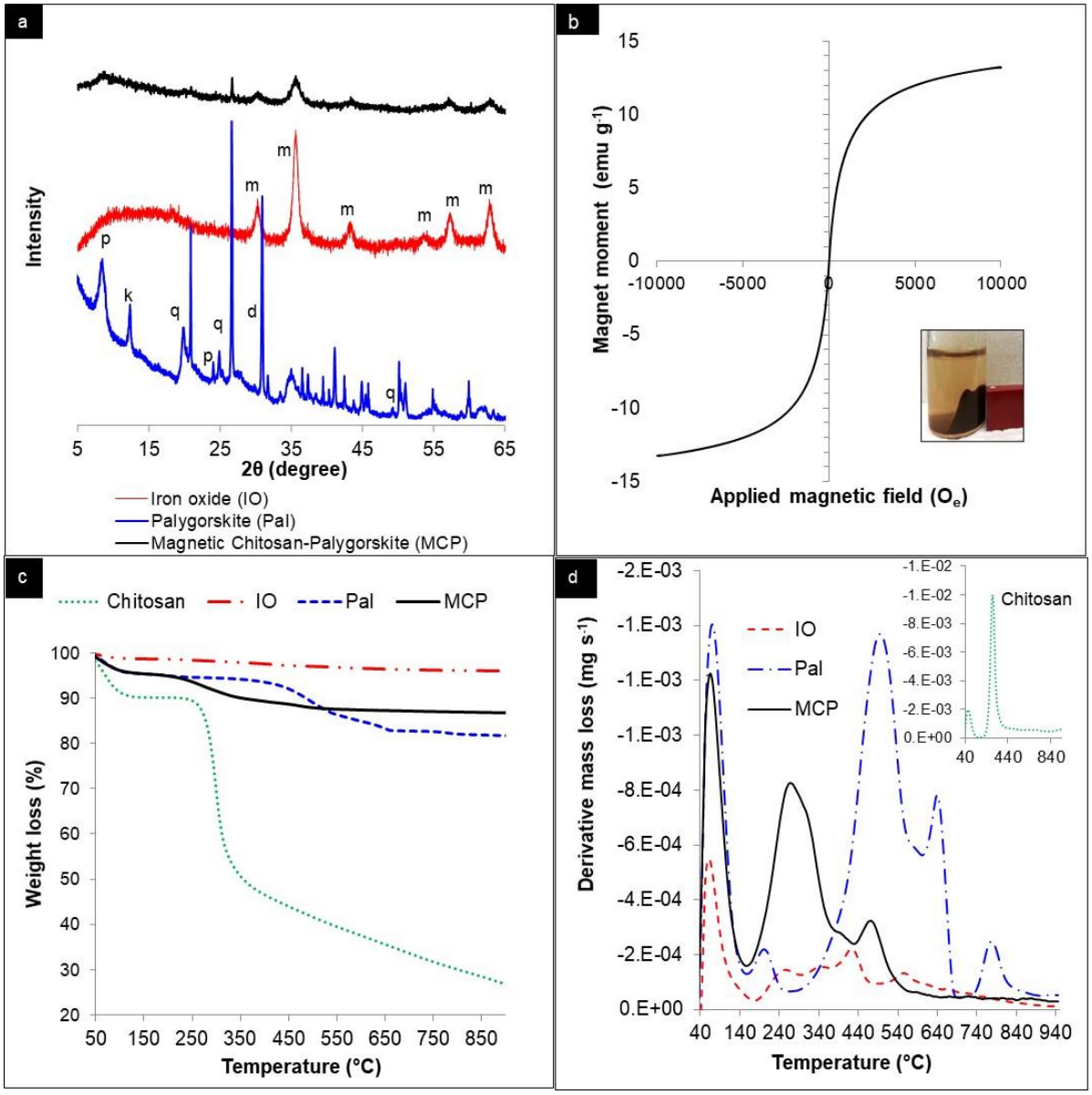

868
869 **Fig. 1.**
870

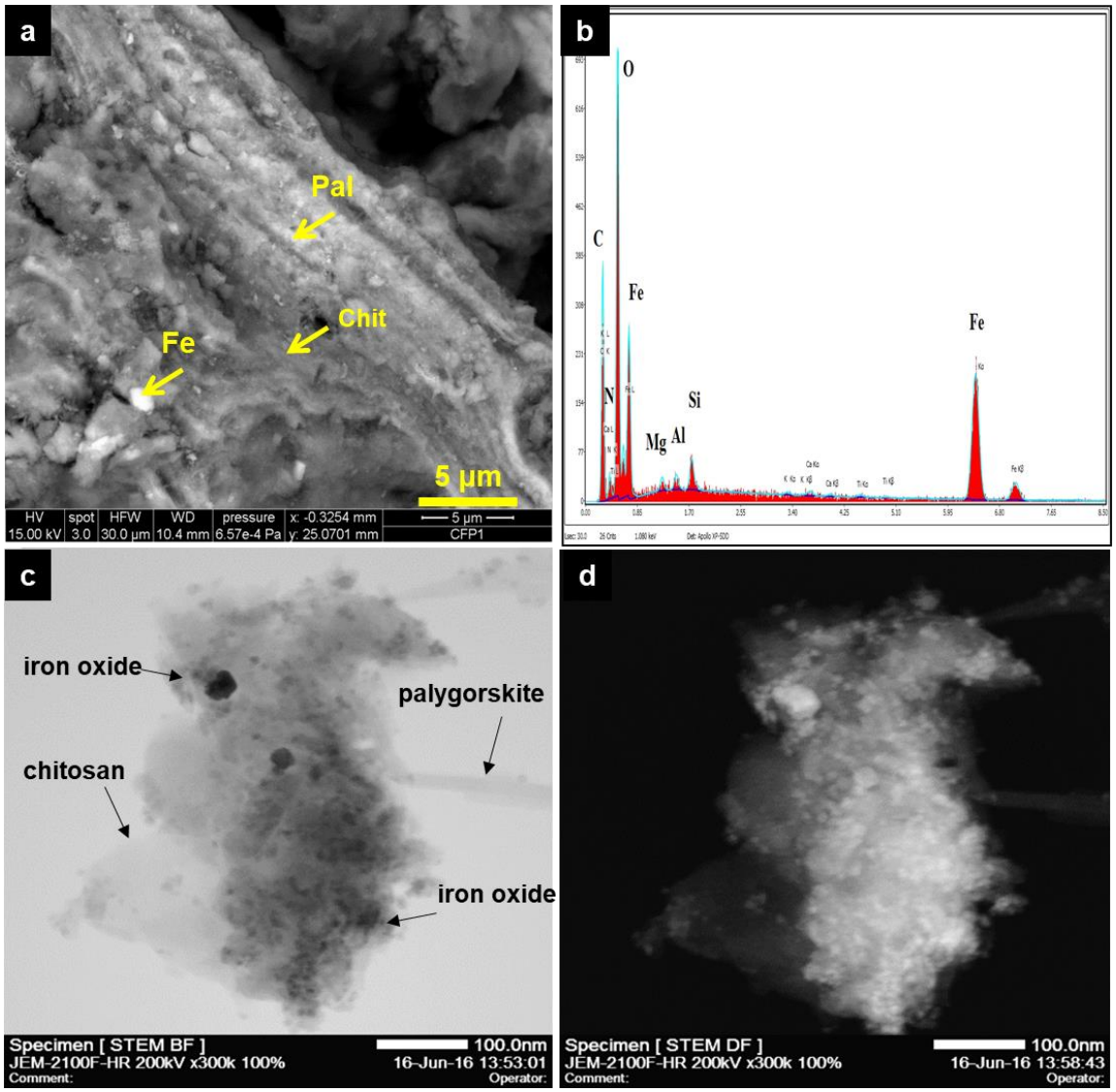

871

872 Fig. 2.

873

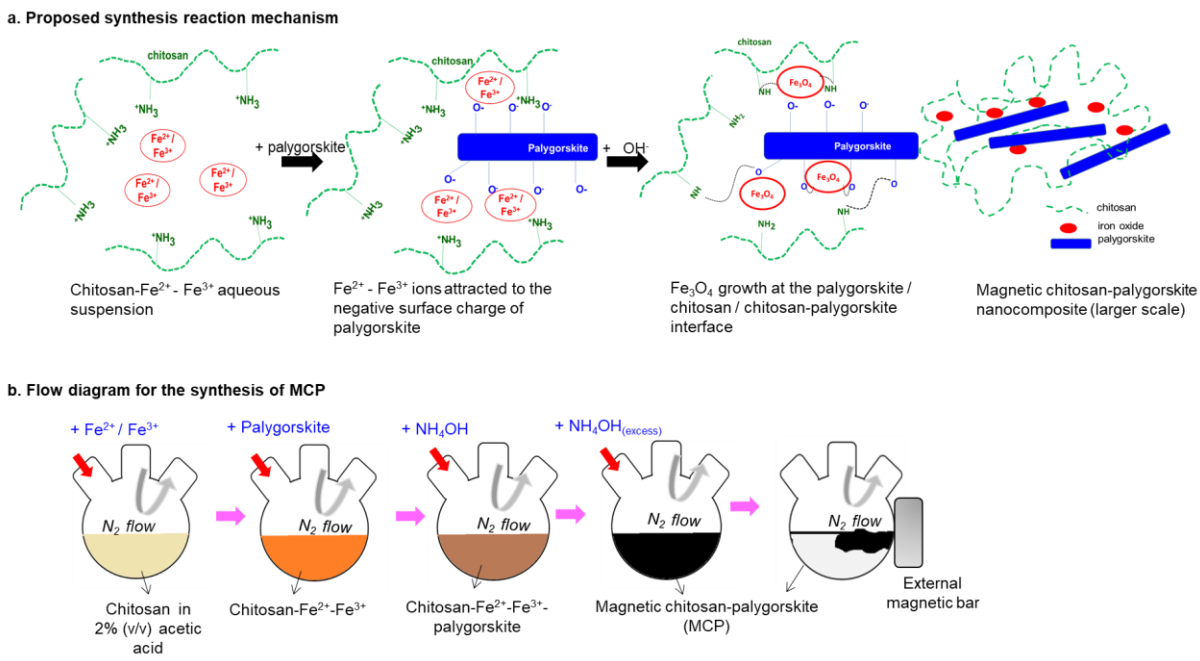

874

875 Fig. 3.

876

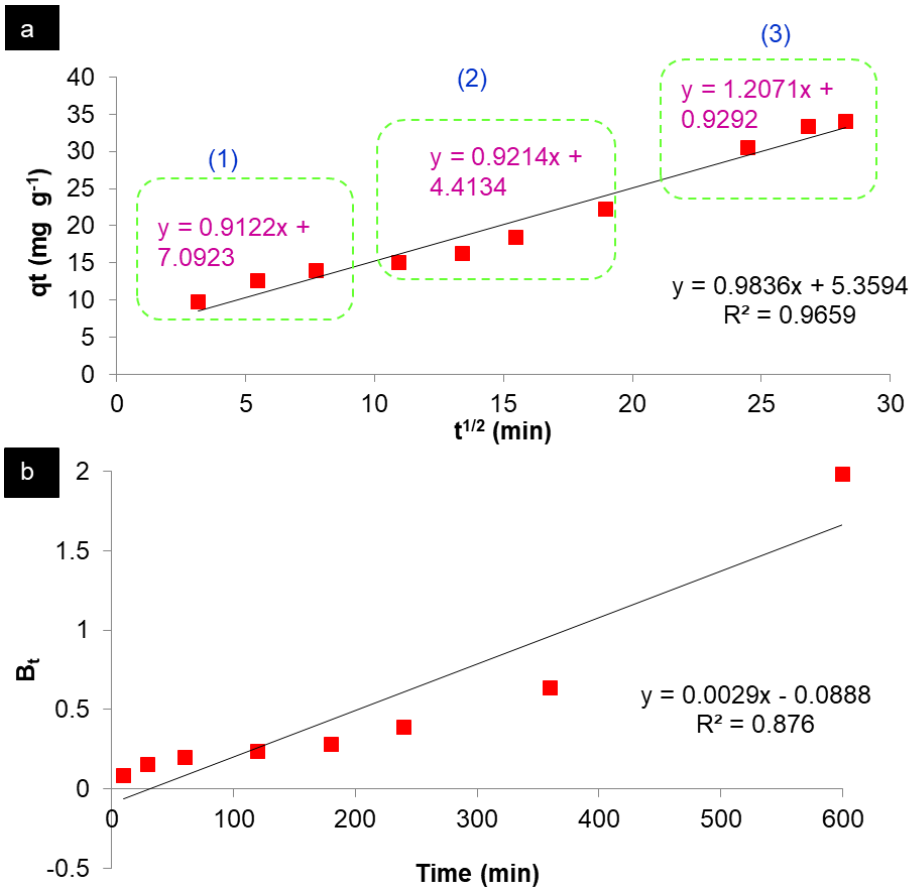

877

878

879 Fig. 4.

880

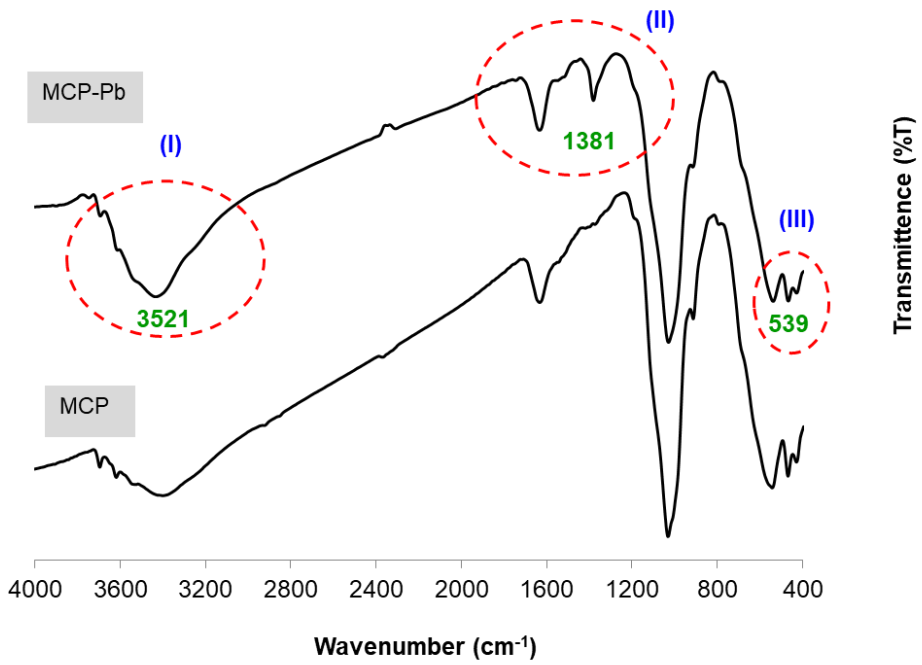

881

882 Fig. 5.

883

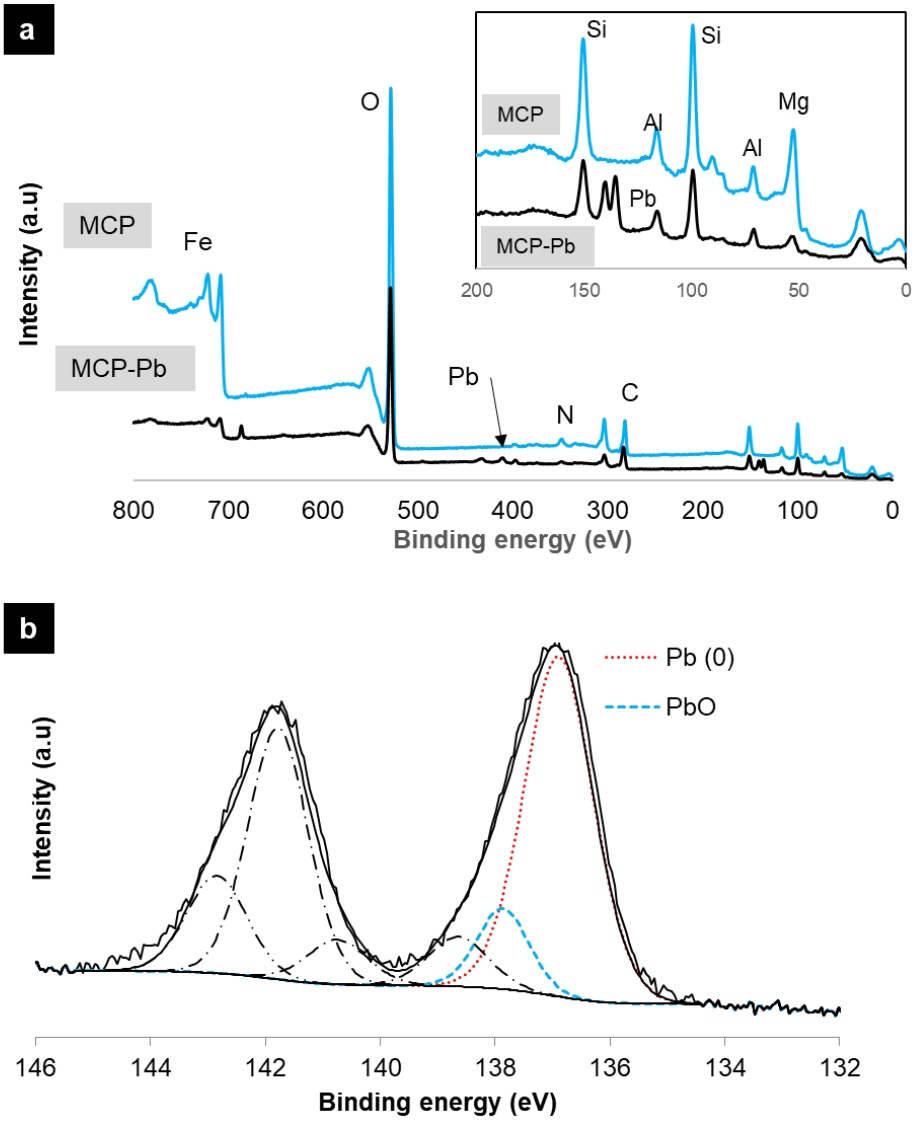

884

885 Fig. 6.

886

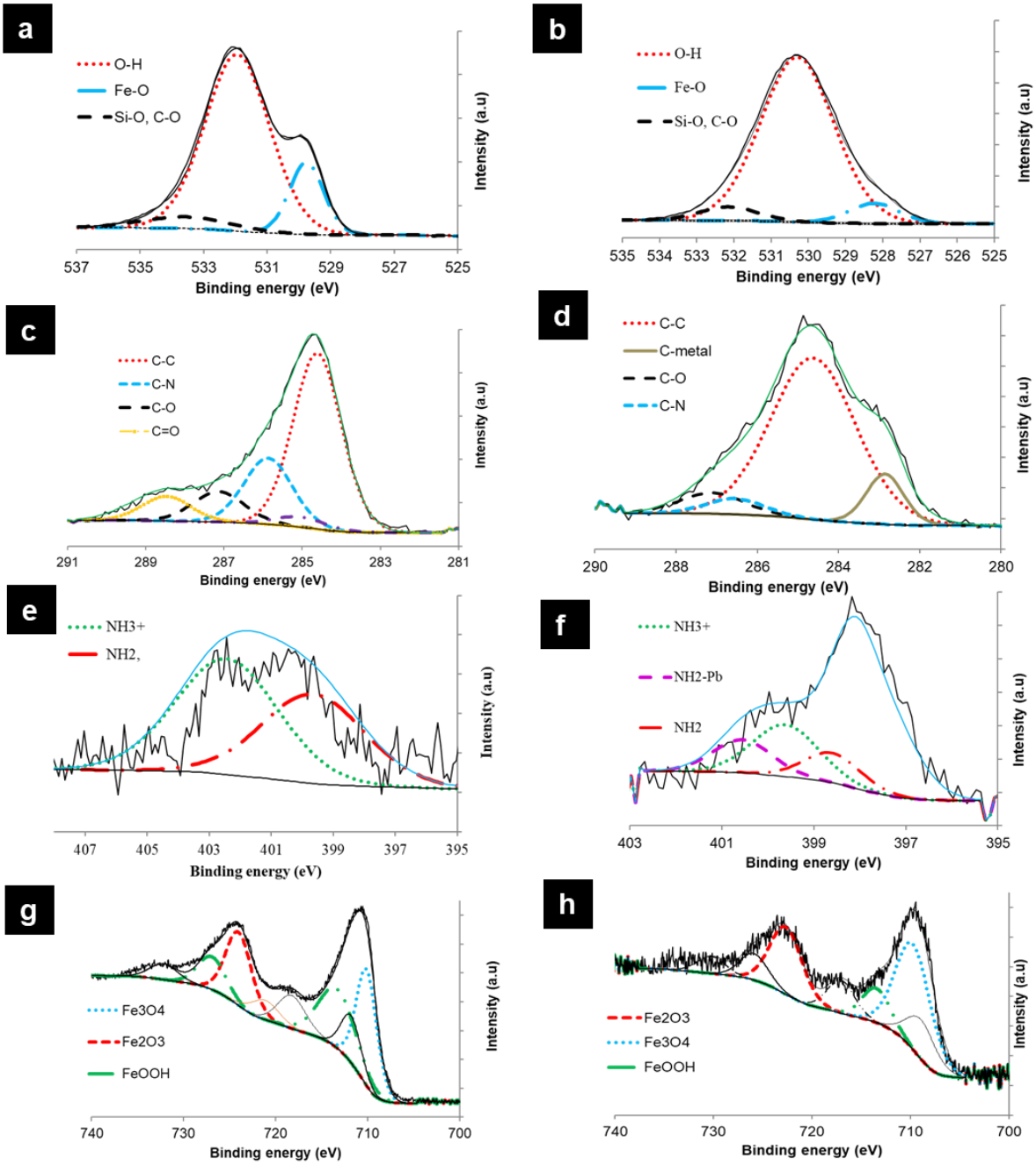

887

888 Fig. 7.

889

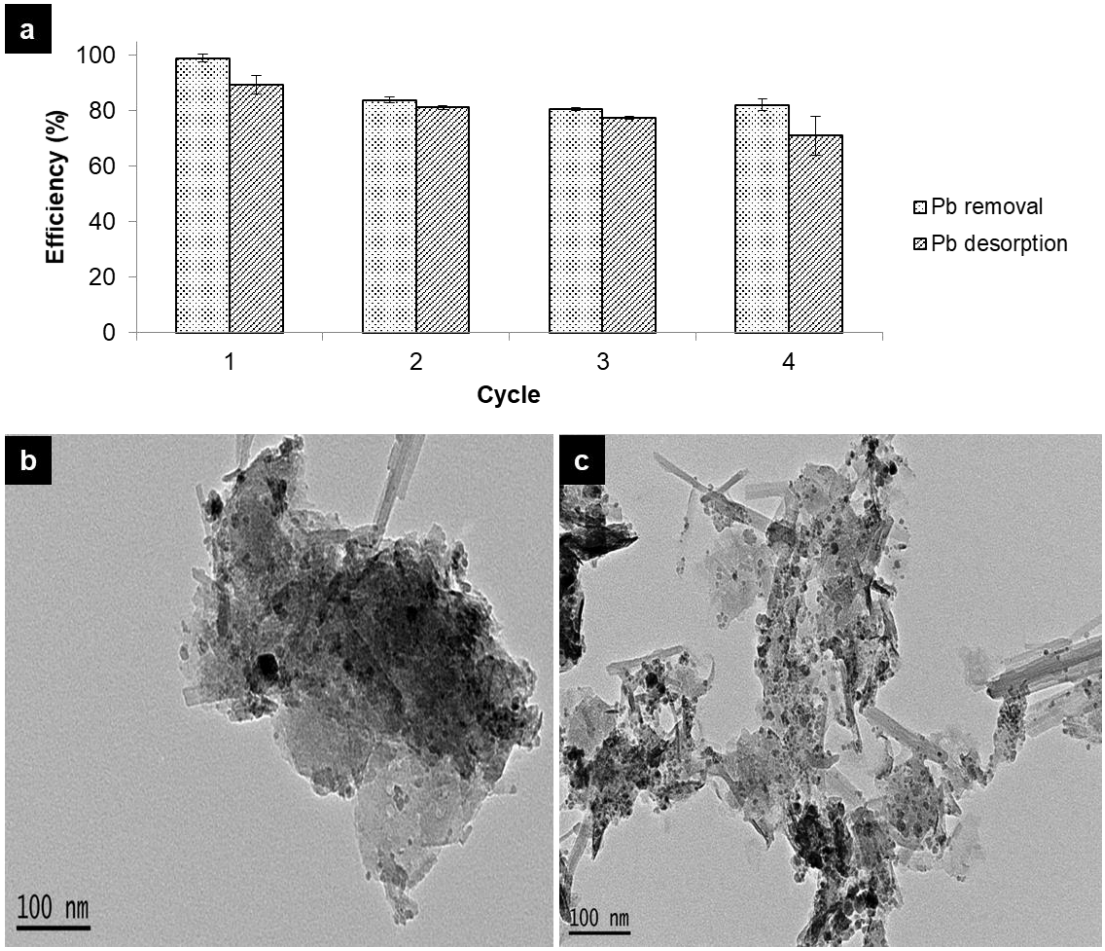

890

891 Fig. 8.

892

893 **Tables**

894 Table 4. Specific surface area, pore volume and pore diameter of palygorskite (Pal), iron

895 oxide (IO) and magnetic chitosan-palygorskite nanocomposite (MCP).

Parameter	Pal	IO	MCP
Specific surface area ($m^2 g^{-1}$)	49.4	72.6	18.3
Average pore volume ($cm^3 g^{-1}$)	0.127	0.215	0.038
Average pore size (Å)	93.0	100	82.1

896

897 Table 5. Langmuir, Freundlich, Dubinin–Radushkevich and Temkin model parameters for

898 Pb^{2+} adsorption by magnetic chitosan-palygorskite nanocomposite (MCP) ($p < 0.05$, n = 2).

Models/parameters	Value
Langmuir	
q_{max} calculated (mg g^{-1})	63.3
K_L (L mg^{-1})	0.0524
R^2	0.9855
q_{max} (experimental) (mg g^{-1})	58.5
Freundlich	
K_F (L g^{-1})	9.415
N	2.846
R^2	0.9820
Dubinin-Radushkevich (D-R)	
q_{max} (mg g^{-1})	91.4
β (x 10^{-9} mol^2J^{-2})	3.00
E (kJ mol^{-1})	12.90
R^2	0.8059
Temkin	
b_T (J mol^{-1})	22.61
A_T (L g^{-1})	0.9087
R^2	0.8708

899

900 Table 6. Adsorption kinetic model parameters of Pb^{2+} adsorption by MCP (initial Pb^{2+}

901 concentration = 200 mg L^{-1}, at 25°C, under 150 agitation per min with 5 g L^{-1} adsorbent

902 loading) at $p < 0.05$, n = 2.

Kinetics models / Parameters	value
Pseudo-first order	
k_1 (min^{-1})	7.60 x 10^{-3}
q_{max} (mg g^{-1})	26.8
R^2	0.9139
Pseudo-second order	
k_2 (g mg min^{-1})	23.6 x 10^{-3}
q_{max} (mg g^{-1})	35.8
R^2	0.9227
Intra-particle diffusion	
k_i (mg g^{-1} $min^{0.5}$)	0.9836
C	5.359
R^2	0.9659
Elovich	
α (mg g^{-1} min^{-1})	1.404
β (g mg^{-1})	0.1795
R^2	0.8044

903

904 Table 4. Comparison of the efficiency of Pb^{2+} adsorption by magnetic composites based on important experimental parameters.

Material	Working pH	Adsorbent loading ($g\ L^{-1}$)	Initial Pb^{2+} concentration ($mg\ L^{-1}$)	Maximum adsorption capacity ($mg\ g^{-1}$)	Magnetic susceptibility ($emu\ g^{-1}$)	Total regeneration cycles and percent removal (%) at the cycle end	Reference
Chitosan-graft-polyacrylamide magnetic composite microspheres	5	10	200	63.7	7.60	N/G*	[78]
Chitosan-magnetite	6	0.1	50 – 80	63.3	55.0	N/G	[79]
Magnetic chitosan nanocomposite	4	3.0	10	3.16	74.0	6 cycles, 93%	[80]
Magnetic Chitosan /graphene oxide composites	5	8.0	N/G	76.9	39.6	5 cycles, 75%	[81]
Palygorskite-iron oxide nanocomposite	5	5.0	20 – 500	26.6	18.3	3 cycles, 64%	[23]

Polyamide−amine dendritic magnetic halloysite nanotubes	5.6	0.5	50 – 200	194	~3.0	8 cycles, 90.6%	[82]
Magnetic nanoparticles coated montmorillonite	6.5	0.002	N/G	38.2	15.0	5 cycles, N/G	[83]
hydroxyapatite-magnetite-bentonite composite	8	2.0	20 – 2100	404	13.2	5 cycles, 86%	[84]
Magnetic sepiolite Clay	6	2.5	N/G	96.2	28.1	5 cycles, ~80%	[85]
Magnetic kaolinite clay	6	1.0	10 – 70	30.9	N/G	N/G	[86]
Magnetic chitosan - palygorskite	4	5.0	50 – 500	58.5	14.3	4 cycles, 82%	This study

905

906 *N/G: Not given.

907

908 Supplementary Data for:

909 **Facile one pot preparation of magnetic chitosan-palygorskite nanocomposite for**

910 **efficient removal of lead from water**

911

912 Ruhaida Rusmin[a,b]*, Binoy Sarkar[c]*, Raj Mukhopadhyay[d], Takuya Tsuzuki[e], Yanju Liu [f,g],

913 Ravi Naidu[f,g]

914

915 [a] Faculty of Applied Sciences, Universiti Teknologi MARA, Negeri Sembilan Branch, Kuala

916 Pilah Campus, 72000 Kuala Pilah, Negeri Sembilan, Malaysia

917 [b] Future Industries Institute, University of South Australia, Mawson Lakes, SA 5095,

918 Australia

919 [c] Lancaster Environment Centre, Lancaster University, Lancaster, LA1 4YQ, UK

920 [d] Division of Irrigation and Drainage Engineering, ICAR-Central Soil Salinity Research

921 Institute, Karnal – 132001, Haryana, India

922 [e] Research School of Engineering, College of Engineering and Computer Science, Australian

923 National University, Acton, ACT 2601, Australia

924 [f] Global Centre for Environmental Remediation, The University of Newcastle, Callaghan,

925 NSW 2308, Australia

926 [g] Cooperative Research Centre for Contamination Assessment and Remediation of the

927 Environment, ATC Building, Callaghan, NSW 2308, Australia

928

929 *Co-corresponding authors: b.sarkar@lancaster.ac.uk (B. Sarkar), ruhaida@uitm.edu.my (R.

930 Rusmin)

931

SD 1: Adsorption isotherm models

Langmuir isotherm

Langmuir adsorption isotherm is characterized by monolayer adsorption of adsorbate on a homogeneous adsorbent surface [1]. The Langmuir isotherm is expressed by the equations 1 and 2:

$$q_e = (K_L\ C_e\ q_m)/(1 + K_L\ C_e) \quad \text{(Eq. 1)}$$

$$C_e/q_e = 1/(K_L\ q_m) + C_e/q_m \quad \text{(Eq. 2)}$$

where, q_e is the amount of adsorbate adsorbed per unit mass of adsorbent (mg g^{-1}); C_e is the equilibrium adsorbate concentration (mg L^{-1}). K_L and q_m are Langmuir constants which stand for bonding energy constant (L mg^{-1}) and maximum monolayer adsorption (mg g^{-1}), respectively. By plotting C_e/q_e versus C_e, the obtained slope of this plot gives $1/q_m$ and intercept gives $1/q_mK_L$. Hence, we calculated the Langmuir constant values from the slope and intercept of the plot.

Freundlich isotherm

The Freundlich isotherm is an exponential expression which suggest that amount of adsorption increases with increase in adsorbate concentration [2]. The Freundlich isotherm is more suitable for heterogeneous adsorbent surface which is expressed by equations 3 and 4:

$$q_e = K_F\, C_e^{1/n} \quad \text{(Eq. 3)}$$

$$\ln q_e = \ln K_F + \frac{1}{n}(\ln Ce) \quad \text{(Eq. 4)}$$

where, q_e is the amount of adsorbate adsorbed per unit mass of adsorbent (mg g^{-1}); C_e is the equilibrium adsorbate concentration (mg L^{-1}). K_F [(mg g^{-1}) (L $mg^{-1})^{1/n}$] and 1/n are Freundlich constant at equilibrium and exponential factor, respectively. By plotting ln q_e versus ln C_e, Freundlich constants values were calculated from slope 1/n and intercept ln K_F.

Dubinin- Radushkevich (D-R) isotherm

The D-R model is able to distinguish the nature of metal adsorption either physical or chemical [3] by measuring the mean free energy, *E* (the free energy of transfer of 1 mole of solute from infinity in solution to the surface of adsorbent).

The D-R model constant, β ($mol^2\ J^{-2}$), is determined by equations 5 and 6 [4]:

$$\ln q_e = \ln q_{max} - \beta\varepsilon^2 \qquad \text{(Eq. 5)}$$

$$\varepsilon = RT \ln\left[1 + \left(\frac{1}{C_e}\right)\right] \qquad \text{(Eq. 6)}$$

where, q_e is the amount of metal adsorbed at equilibrium (mg g^{-1}) and q_{max} is the maximum adsorption capacity (mg g^{-1}). Meanwhile R, T, and Ɛ is the gas constant (8.314 J $mol^{-1}\ K^{-1}$), temperature (K) and the Polanyi potential ($J^2\ mol^{-2}$), respectively. The β and q_{max} can be calculated from the slope and intercept of the D-R model plot.

The relationship between the β value and mean free energy of adsorption (*E*) (kJ mol^{-1}) is derived from equation 7:

$$E = -\frac{1}{\sqrt{2\beta}} \qquad \text{(Eq. 7)}$$

Temkin isotherm

Temkin isotherm model considers the interaction effect between adsorbate and adsorbent on adsorption phenomenon. The model suggests that heat of adsorption would decrease linearly with surface coverage due to the adsorbate-adsorbent interaction [5].The Temkin isotherm can be expressed by equations 8 and 9:

$$q_e = (RT/b_T) \ln (A_T C_e) \qquad \text{(Eq. 8)}$$

$$q_e = B \ln A_T + B \ln C_e \qquad \text{(Eq. 9)}$$

where, q_e is the amount of adsorbate adsorbed per unit mass of adsorbent (mg g^{-1}), B = RT/b_T, b_T is the Temkin constant related to heat of sorption (J mol^{-1}), A_T is the Temkin isotherm constant (L g^{-1}), R is the gas constant (8.314 J. mol^{-1} K^{-1}), and T is the absolute temperature (K).

SD2: Adsorption kinetic models

Pseudo-first order kinetic model

The assumption of this model is the sorption rate abates linearly with the adsorption capacity [6]. It is expressed by the equations below:

$$q_t = q_e (1 - e^{-k_1 t}) \quad \text{(Eq. 10)}$$

$$\ln (q_e - q_t) = \ln q_e - k_1 t \quad \text{(Eq. 11)}$$

where, q_e and q_t are the amount of adsorption at equilibrium and time t, respectively (mg g^{-1}), k_1 is the rate constant of pseudo first-order adsorption (min^{-1}). By plotting ln (q_e- q_t) versus t, we obtained the slope k_1 and intercept ln q_e.

Pseudo-second order kinetic model

The pseudo-second-order kinetic model is usually utilized to elucidate a chemical sorption and it considers the rate-limiting step is the interaction between two reagent particles [7]. It is expressed by the equations below:

$$q_t = q_e^2 k_2 t / 1 + q_e k_2 t \quad \text{(Eq. 12)}$$

$$t/q_t = 1/k_2 q_e^2 + t/q_e \quad \text{(Eq. 13)}$$

where, q_e and q_t are the amount of adsorption at equilibrium and time t, respectively (mg g^{-1}), k_2 is the rate constant of pseudo first-order adsorption (g mg^{-1} min^{-1}). By plotting t/q_t versus t, we obtain the slope $1/q_e$ and intercept $1/k_2 q_e^2$.

Intra-particle diffusion model

Intra-particle diffusion model is characterized by diffusion where the adsorption process is dependent upon speed of adsorbate diffusion through adsorbent [8]. By plotting q_t versus $t^{0.5}$, we obtain the constant k_i (mg $g^{-1}min^{-1/2}$) from slope and C (mg g^{-1}) from the intercept.

$$q_t = k_i t^{1/2} + C \quad \text{(Eq. 14)}$$

Elovich model

Elovich model is characterized by chemisorption nature of adsorption kinetic process related to surface coverage [9] and expressed by the equations 15 and 16. By plotting q_t versus ln (t), we obtain the slope 1/β and intercept 1/β ln (αβ).

$$dq_t/dt = \alpha e^{-(\beta . qt)} \quad \text{(Eq. 15)}$$

$$q_t = 1/\beta \ln (\alpha\beta) + 1/\beta \ln (t) \quad \text{(Eq. 16)}$$

where, q_t is the sorption capacity at time t (mg g^{-1}), α is the initial sorption rate (mg g^{-1} min^{-1}), and the parameter β is related to the extent of surface coverage and activation energy for chemisorption (g mg^{-1}).

Boyd model

The model was expressed as a function of F, described as the fraction of solute adsorbed at a specific time (q_t, mg g^{-1}) and at equilibrium (q_e, mg g^{-1}), calculated through the expression F = q_t/q_e.

The Boyd parameter (B_t) could be determined through equations 17 or 18, depending on the value of F [10].

$$\text{For } F < 0.85: \; B_t = 2\pi - \frac{\pi^2 F}{3} - 2\pi\left(\frac{1-\pi F}{3}\right)^{1/2} \quad \text{(Eq. 17)}$$

$$\text{For } F > 0.85: \; Bt = -\ln (1- F) - 0.4977 \quad \text{(Eq. 18)}$$

SD3: Thermodynamic analysis

The standard Gibbs free energy change of adsorption (ΔG°) (sup info) was determined by the classic Van't Hoff equation (equation 19):

$$\Delta G^{o} = -RT\ln K \quad \text{(Eq. 19)}$$

where, R is the universal gas constant (8.314 J $mol^{-1}K^{-1}$) and K is the equilibrium constant at the temperature T (K). K_D, a distribution coefficient constant (dimensionless) was used to represent the K [11] and was calculated through equation 20:

$$K_D = \frac{q_e}{C_e} \quad \text{(Eq. 20)}$$

where q_e and C_e is respectively the equilibrium adsorption capacity (mg g^{-1}) and concentration at equilibrium (mg L^{-1}). By using a derivative Van't Hoff equation (equation 21), the standard enthalpy of adsorption (ΔH°) and entropy of adsorption (ΔS°) were determined through plotting ln K_D versus 1/T [11]. From this graph, the magnitude of ΔH° was calculated from the slope, while ΔS° was derived from the intercept.

$$\ln K_D = \frac{\Delta S^{o}}{R} - \frac{\Delta H^{o}}{RT} \quad \text{(Eq. 21)}$$

Supplementary figures

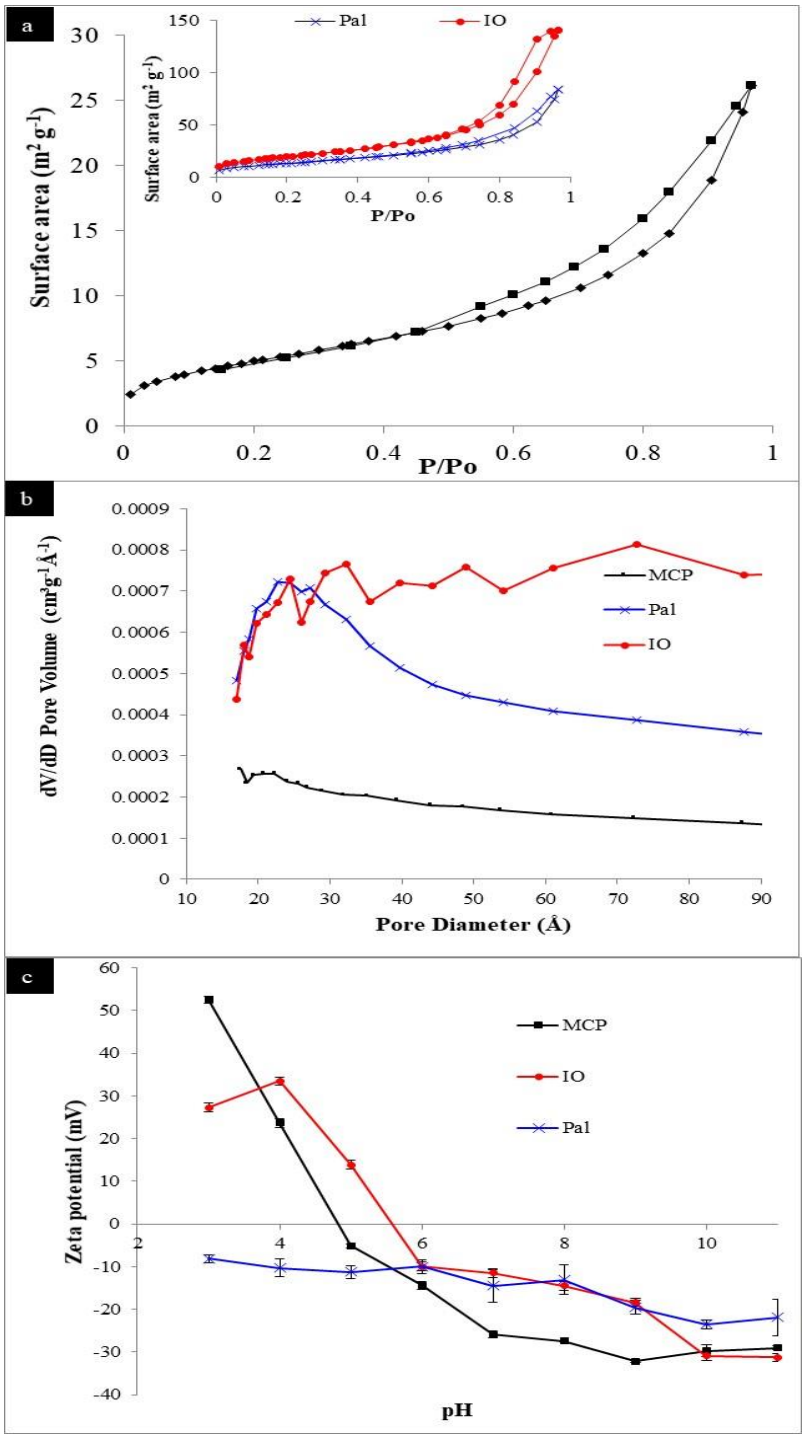

Fig. S1. N_2 adsorption-desorption isotherm (a), pore size distribution (b), and zeta potential values (c) of magnetic chitosan-palygorskite composite (MCP), iron oxide (IO) and palygorskite (Pal). Error bars represent standard error at 95% confidence level, n = 2.

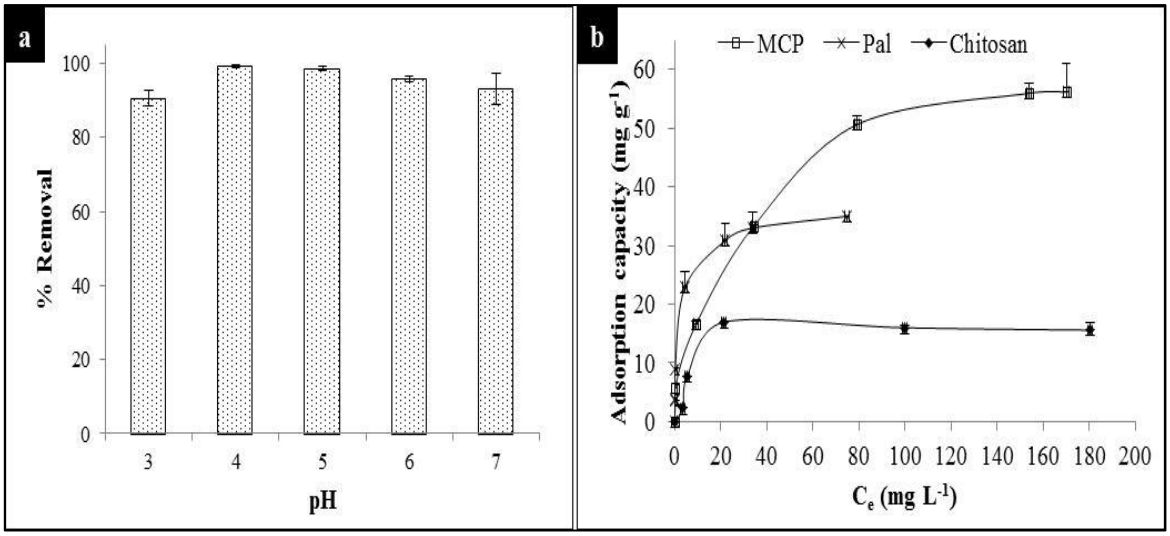

Fig. S2. Adsorption of Pb^{2+} on MCP: (a) influence of pH on Pb^{2+} removal (at initial Pb^{2+} concentration of 50 mg L^{-1}), (b) adsorption isotherms of MCP, palygorskite (Pal) and chitosan (at 25°C with 150 agitations per min and 5 g L^{-1} adsorbent loading) (Error bars represent standard error at 95% confidence level, n = 2).

Supplementary tables

Table S1. Thermodynamic parameters of Pb^{2+} adsorption by MCP at different temperatures and initial concentrations

Initial $[Pb^{2+}]$ ($mg\ L^{-1}$)	Adsorption capacity ($mg\ g^{-1}$)			ΔG° (kJ mol^{-1})			ΔH° (kJ mol^{-1})	ΔS° (J $mol^{-1}\ K^{-1}$)
	25°C	40°C	55°C	25°C	40°C	55°C		
50	5.74	7.01	12.3	-103	-108	-113	118	346
100	16.6	21.2	22.1	-29.4	-30.9	-32.4	40.9	98.8
200	33.3	38.2	35.6	-11.3	-11.9	-12.4	25.8	38.0

References

[1] I. Langmuir, The constitution and fundamental properties of solids and liquids, J. Am. Chem. Soc. 38 (1916) 2221–2295.

[2] H. Freundlich, Adsorption in solution, Phys. Chemie. 57 (1906) 384–410.

[3] M.M. Dubinin, The potential theory of adsorption of gases and vapors for adsorbents with energetically non-uniform surface, Chem. Rev. 60 (1960) 235–266.

[4] K. Y. Foo, B. H. Hameed, Insights into the modeling of adsorption isotherm systems, Chem. Eng. J. 156 (2010) 2-10.

[5] M.J. Temkin, V. Pyzhev, Recent modifications to Langmuir isotherms, Acta Physiochim U.R.S.S. 12 (1940) 217–222.

[6] L.D. Hafshejani, A. Hooshmand, A.A. Naseri, A.S. Mohammadi, F. Abbasi, A. Bhatnagar, Removal of nitrate from aqueous solution by modified sugarcane bagasse biochar, Ecol. Eng. 95 (2016) 101–111.

[7] F. Zhang, J. Lan, Y. Yang, T. Wei, R. Tan, W. Song, Adsorption behavior and mechanism of methyl blue on zinc oxide nanoparticles, J. Nanoparticle Res. 15 (2013) 2034.

[8] W.J. Weber, J.C. Morris, Kinetics of adsorption on carbon from solution, J. Sanit. Eng. Div. 89 (1963) 31–59.

[9] S. Z. Roginsky, J. Zeldovich, An equation for the kinetics of activated adsorption, Acta Physicochim U.S.S.R. 1 (1934) 554-559.

[10] B. H. Hameed, M. I. El-Khaiary, Malachite Green adsorption by rattan sawdust: Isotherm, kinetic and mechanism modelling, J. Hazard Mater. 159 (2008) 574-579.

[11] C. R. T. Tarley, F. N. Andrade, H. d. Santana, D. A. M. Zaia, L. A. Beijo, M. G. Segatelli, Ion-imprinted polyvinylimidazole-silica hybrid copolymer for selective extraction of Pb(II): Characterization and metal adsorption kinetic and thermodynamic studies, React. Funct. Polym. 72 (2012) 83-91.